APPLIED PHYSICS REVIEWS—FOCUSED REVIEW

Small-angle neutron scattering in materials science: Recent practical applications

Yuri B. Melnichenko[a] and George D. Wignall
Neutron Scattering Sciences Division, Oak Ridge National Laboratory, Oak Ridge, Tennessee 37831

(Received 8 January 2007; accepted 2 April 2007; published online 25 July 2007)

Modern materials science and engineering relies increasingly on detailed knowledge of the structure and interactions in "soft" and "hard" materials, but there have been surprisingly few microscopic techniques for probing the structures of bulk samples of these substances. Small-angle neutron scattering (SANS) was first recognized in Europe as a major technique for this purpose and, over the past several decades, has been a growth area in both academic and industrial materials research to provide structural information on length scales ~10–1000 Å (or 1–100 nm). The technique of ultrahigh resolution small-angle neutron scattering (USANS) raises the upper resolution limit for structural studies by more than two orders of magnitude and (up to ~30 μm) and hence overlaps with light scattering and microscopy. This review illustrates the ongoing vitality of SANS and USANS in materials research via a range of current practical applications from both soft and hard matter nanostructured systems. © *2007 American Institute of Physics*. [DOI: 10.1063/1.2759200]

TABLE OF CONTENTS

I. INTRODUCTION

Many of the powerful techniques developed to study materials in the past few decades are rendered intractable by their very power when applied to materials of the complexity of a polymer alloy, colloidal suspension, or a microporous medium; they yield information in such detail that the features which make the bulk material interesting are obscured in the mass. What is often required is a probe which is sensitive to possibly new features in the microscopic structure while remaining insensitive to those aspects of the structure which are essentially common to the class of materials being studied. In considering a blend of two known polymers, for example, a technique such as conventional crystallography provides a wealth of information on the (already known) atomic structure of the chemical monomers, buried in which may be new information on whether or not the blend is actually thermodynamically stable.

Small-angle neutron scattering (SANS) is a technique in which the microscopic length scale probed in the sample may be chosen to suit the property being studied while remaining insensitive to much finer or much coarser details. Since most materials are essentially transparent to neutrons of the wavelengths typically used (~5–20 Å), bulk samples may be studied, and sample environments are easily varied over a wide range of pressures and temperatures. Further, the need to site these instruments at suitable pulsed or steady-state (reactor) sources has offered SANS users routine access to state-of-the-art centralized facilities such as millikelvin refrigerators or high-field cryomagnets. For these and other reasons, SANS has become very widely used in the study of, *inter alia*, polymers, colloids, metals, glasses, gels, ceramics, biological macromolecules, and micellar and microemulsion systems. We shall attempt here to illustrate the continued vitality of small- and ultrasmall-angle scattering techniques via a range of current practical applications from both "soft" and "hard" matter nanostructured systems.

[a]Electronic mail: yui@ornl.gov

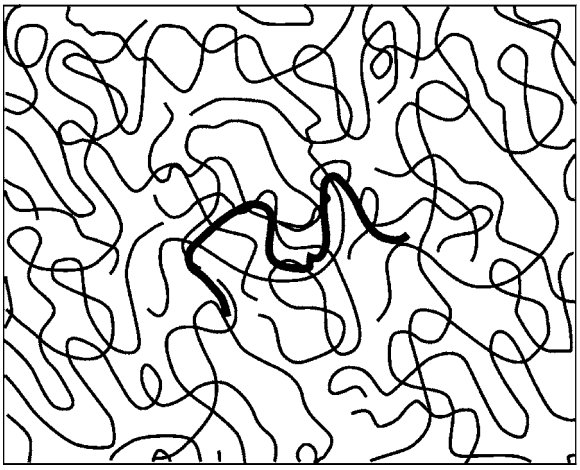

FIG. 1. Schematic configuration of polymer molecules showing how deuterium labeling can be used to "stain" individual molecules and make them "visible" in the condensed state or concentrated (overlapping) polymer solutions via small angle neutron scattering.

Real materials seldom consist of a single crystal, and their behavior is profoundly affected by the detailed nature of their internal disorder. In metals and ceramics, for example, a considerable amount of research is concerned with microstructural changes induced by stress, radiation damage, nucleation, and growth stages during heat treatments or void development during deformation. One feature of using SANS for such studies is the ability to measure *in situ*, which alleviates the need to work with quenched or sliced samples when such a procedure is undesirable.

Polymers provide an especially rich field for SANS studies, not least because of the ability to exploit a technique known as contrast variation, which is based on the fact that each elemental isotope exhibits a different refractive index for neutrons. The configuration of a single type of polymer chain, for example, may thus be observed in a bulk polymer blend by deuterating only the chains of interest in an otherwise protonated system, as illustrated schematically in Fig. 1.

This ability to determine the size, shape, and interactions of polymer molecules in real materials stands at the very heart of polymer science and engineering, especially in view of ongoing trends toward the production of polymer alloys rather than the synthesis of new species of macromolecules. Extensive investigations of blend compatibility have been undertaken by SANS, which is the only technique available to determine separation or intermixing at the segmental level, and a broad review of the general field has recently been given.[1] Such materials currently account for a growing fraction (approximately one-third) of the polymer market, so these materials have been the subject of extensive scientific and commercial interest. SANS has developed into a powerful method for the study of their structure and interactions and has had a great impact on the field by providing detailed thermodynamic information at the molecular level. Because these developments have important applications in materials science, SANS has been widely used by industrial scientists.[2–6]

Colloidal dispersions and suspensions of immense variety are ubiquitous throughout materials science, and SANS has been widely applied in the study of such multiphase systems, which typically exhibit spatial correlations over distances $\sim 1-100$ nm, corresponding to the size of individual particles (e.g., micelles and microemulsions droplets) or to the range of interactions between particles (e.g., polymer latexes). These dimensions, coupled with the fact that most colloids and/or the media in which they are suspended contain copious amounts of hydrogen (so they are suitable for applying deuterium-labeling techniques), make SANS a technique of choice for structural studies.[7] Reviews of such applications to colloids in water- and oil-based media have been given by Hayter and Penfold,[8] Hayter,[9] Magid,[10] and Chen.[11]

II. SANS ESSENTIALS

A. Deuterium labeling and neutron contrast

Over the past several decades, new synthetic products based on polymers, colloids, and gels have replaced many natural commodities such as silk, cotton, and wood. A common characteristic of many such materials is the size of the molecules that form them, which are made by bonding together many (poly) smaller molecules (monomers), that consist of atoms such as hydrogen, carbon, and oxygen. The "mers," or segments, are linked together in the same giant macromolecule, in much the same way that toy "poppet" beads can be strung together to make a child's necklace. For example, typically $\sim 10^3$ ethylene (C_2H_4) units are bonded together to make polyethylene, the familiar plastic that we experience in everyday use (e.g., in milk jugs, garbage bags, packaging). Thus, understanding the basic organization of such "macromolecules" is a necessary prerequisite for controlling their behavior, and scattering techniques have been employed since the beginning of polymer science to provide such information.

The first studies of polymer chain configurations were made via light and small-angle x-ray scattering, and the methodology to measure the chain dimensions, virial coefficients and molecular weights was established in the classical works of Zimm,[12] Guinier and Fournet,[13] Debye[14] and Kratky,[15] who pioneered these techniques. These experiments were usually conducted in dilute solution due to the difficulties of separating the *interchain* and *intrachain* contributions to the structure, which could only be done in the limit of zero concentration.

The application of scattering techniques to measure chain dimensions in concentrated solutions and the condensed state was eventually made possible[16,17] by taking advantage of the difference in the coherent scattering length between deuterium ($b_D = 0.66 \times 10^{-12}$ cm) and hydrogen ($b_H = -0.37 \times 10^{-12}$ cm), which results in a marked difference in scattering power (contrast) between molecules synthesized from normal (hydrogenous) and deuterated monomer units. Thus, deuterium-labeling techniques may be used to "stain" molecules and make them "visible" in the condensed state and other crowded environments, such as concentrated

solutions of overlapping chains, as illustrated schematically in Fig. 1. Following the development of the first instruments[18,19] suitable for this type of structural analysis, the technique has been widely applied to elucidate the arrangements of macromolecules in the condensed state.

As mentioned above, scattering techniques have been employed since the beginning of polymer science to provide information on the spatial arrangements of macromolecules in dilute solution[12–15] and to determine crystal structures[20–22] via x rays using Bragg's law

$$\lambda = 2D \sin \theta, \tag{1}$$

where D is the distance between crystallographic planes, λ is the wavelength, and 2θ is the angle of scatter. For elastic scattering (where the energies of the incident and scattered neutrons are the same), the intensity is measured as a function of the momentum transfer

$$Q = 4\pi\lambda^{-1} \sin \theta. \tag{2}$$

Combining Eqs. (1) and (2) gives $D=2\pi/Q$, so in order to study the length scales (1–100 nm) that are important for polymers (e.g., the size of the polymer "coil"), we need to work at low Q values ($\sim 10^{-3} < Q < 0.1$ Å^{-1}) and collect data at small angles ($\theta < 10°$) using long wavelength ($5 < \lambda < 20$ Å) or "cold" neutrons.

SANS has proven to be one of the most important tools for the evaluation of polymer chain conformation. This is because neutrons are scattered differently by hydrogen (H^1) and deuterium (D^2), and this property is important because the scattering of an object depends on the difference between the particle and its environment. Thus, one way to create such a difference (contrast) is to deuterate or isotopically "color" or stain individual chains or parts of molecular aggregates to make them visible in the condensed state. This process is illustrated schematically in Fig. 1 and the combination of SANS and D^2-labeling techniques has been able to answer many long-standing questions concerning the way in which polymer molecules pack together and to measure their dimensions. For the typical polyethylene chain mentioned above, ~4000 ethylene (C_2H_4) units (segments) are covalently bonded together to give an overall (weight-averaged) molecular weight, $M_w \sim 10^5$. The average size of the chain (or radius of gyration) is $R_g \sim 140$ Å, so the molecule pervades a volume of $(4\pi/3)R_g^3 \sim 10^8$ Å^3, whereas the molecule itself occupies a volume of only $\sim 2\times 10^5$ Å^3. It follows that the space penetrated by the molecule is shared with ~500 other chains, all of which are entangled and intertwined together. Thus, a typical segment can interact with 4000 segments on the same chain and with 500 other chains, each of which contains another 4000 segments. This illustrates the difficulty of calculating the chain trajectory, which is truly a many-body problem that would be hard to address, even with the massive computing power which is available today. Figure 1 indicates schematically the great simplification provided by SANS, which is able to measure the actual configuration of a particular polymer molecule. We can define a coherent scattering length of the repeat monomer unit (segment) by

$$b = \sum_k b_k, \tag{3}$$

where b_i is the scattering length of the ith atom in a D^2-labeled monomer unit (b_D), and a similar equation may be written for the coherent scattering length of a H^1-labeled monomer unit (b_H). If the two identical isotopically labeled polymers, with polymerization index (N) and segment (monomer) volume (υ), are blended together so that the volume fraction of H^1- and D^2-labeled components are ϕ_H and ϕ_D, respectively, the differential scattering cross section per unit solid angle per unit sample volume is given[1] by

$$\left[\frac{d\Sigma(\Omega)}{d\Omega}\right] = \upsilon^{-1} N \phi_H \phi_D (b_H - b_D)^2 P(Q), \tag{4}$$

where $d\Sigma(Q)/d\Omega$ is directly analogous to the Rayleigh ratio used in light scattering. After subtracting off an "incoherent background," which is independent of Q to a first approximation and arises mainly from H^1 atoms, and any coherent background signal, the cross section is proportional to $P(Q)$, the single-chain (intramolecular) form factor [$P(0)=1$]. This originates from monomer pairs belonging to the same chain and reflects the configuration of individual molecules.

The quantity $(b_D - b_H)^2$ is related to the difference in scattering power between labeled and unlabeled chains. In general, radiation incident on a medium whose scattering power is independent of position is scattered only into the forward direction ($\theta=0$), and all scattering cancels unless the scattering power fluctuates from point to point in the sample. Neutrons are scattered by nuclei, each of which has a different scattering amplitude, so the contrast arises from fluctuations in scattering length density (SLD), which for polymers is defined as the sum of coherent scattering lengths b [e.g., Eq. (3)], divided by the segment volume (υ): $\rho^* = b/\upsilon$. The coherent cross section of a system of uniform SLD is zero, though fluctuations may be introduced by means of isotopic substitution, thus giving rise to a finite cross section [e.g., Eq. (4)], proportional to $(b_H - b_D)^2$. In general, the neutron contrast factor k_n is defined as

$$k_n = \frac{1}{A_0}\left(\frac{b_A}{\upsilon_A} - \frac{b_B}{\upsilon_B}\right)^2 \sim (\rho_A^* - \rho_B^*)^2, \tag{5}$$

where A_0 is Avogadro's number and ρ_A^* and ρ_B^* are SLDs of the two components in a binary system. Table I gives some of the SLDs or neutron refractive indices for the materials described in this article.

B. Illustrative example using SANS to study single-chain configurations in the condensed state

SANS measurements in dilute solution offer few advantages over light or small-angle x-ray scattering (LS/SAXS) techniques, which permit the elucidation of chain dimensions via the electron density contrast between a macromolecule and a solvent. A greater signal-to-noise ratio may be obtained with the neutron technique,[1] though the main impact of SANS has been in the area of semidilute and concentrated solutions and the technique has provided us with a wealth of information previously unavailable through LS/SAXS,

TABLE I. Neutron scattering length densities of some polymers and solvents (at room temperature except for CO_2).

Polymer segment or solvent molecule	Formula	Scattering length density, ρ^* (10^{10} cm^{-2})
Polystyrene	C_8H_8	1.44
Polystyrene-D8	C_8D_8	6.46
Polyethylene	C_2H_4	–0.28
Polyethylene-D4	C_2D_4	6.78
Water	H_2O	–0.56
Heavy water	D_2O	6.4
Carbon dioxide	CO_2	2.50ρ[a]
H-decane	$C_{10}H_{22}$	–0.49
D-decane	$C_{10}D_{22}$	6.58
H-tetracosane	$C_{24}H_{50}$	–0.39
D-tetracosane	$C_{24}D_{50}$	7.04
H-hexatriacontane	$C_{36}H_{74}$	–0.36
D-hexatriacontane	$C_{36}D_{74}$	7.00
H-*n*-decyl-tetraoxyethylene ($C_{10}E_4$)	$C_{14}H_{26}O_5$	0.18
D-*n*-decyl-tetraoxyethylene ($C_{10}E_4$)	$C_{14}D_{26}O_5$	6.86
H-toluene	C_7H_8	0.94
D-toluene	C_7D_8	5.66
Fullerene	C_{60}	7.53[b]
Carbon disulfide	CS_2	1.24
D-xylene	C_8D_{10}	6.04
D-benzene	C_6D_6	5.42

[a]Here, ρ is the fluid density in g/cm^3.
[b]Using a volume calculated from the van der Waals radii of the crystal, 5.02 Å.

where intermolecular interference restricts measurements to dilute solutions. These effects may be overcome at higher polymer concentrations by SANS measurements on systems where a fraction of the solute is isotopically labeled (Fig. 1).

The first applications of the SANS technique were made in the field of bulk amorphous polymers, where there have been several theoretical approaches to the molecular conformation. The main model has been the unperturbed Gaussian (random) coil due to Flory,[23,24] though others have also been advanced,[1] and before the development of the SANS technique there was no way of directly measuring the molecular conformation in the condensed state. This led to a widespread debate on the issue in the literature, and the first measurements using D^2 labeling to provide a direct determination of scattering function (form factor) describing the single chain, $P(Q)$, were undertaken in the early 1970s.[25–31] Figure 2 shows one of the first quantitative SANS experiments[32] performed in the bulk polymer and gives the scattered intensity for normal hydrogenous polyethylene [$(C_2H_4)_n$ or PEH] and that of a solution of a small amount of deuterated polyethylene [$(C_2D_4)_n$ or PED]. The data in Fig. 2 are given as an absolute cross section per unit volume, $d\Sigma(Q)/d\Omega$, in units of cm^{-1}, which is directly analogous to the Rayleigh ratio used in light scattering studies.[26]

The parameter used to describe the overall size of a polymer chain is called the radius of gyration R_g, which is defined as the root-mean-square distance of all scattering elements from the center of gravity. R_g may be derived by expanding the Debye form factor $P(Q)$ for a Gaussian chain,

$$P(Q) = (2/Q^4R_g^4)[\exp(-Q^2R_g^2) - 1 + Q^2R_g^2], \quad (6)$$

in a power series for low $Q(Q < R_g^{-1})$ and plotting $d\Sigma^{-1}(Q)/d\Omega$ versus Q^2.[12]

Alternatively, these parameters may be obtained by plotting $\ln[d\Sigma(Q)/d\Omega]$ versus Q^2 at low Q.[13] These types of plots are conventionally referred to as Zimm and Guinier plots, respectively, and the former is generally used for investigating polymer configurations as it has been found to be linear over a wider Q range. Figure 3 shows the data of Schelten *et al.*[32] for solutions of PED in PEH, drawn in a Zimm plot,

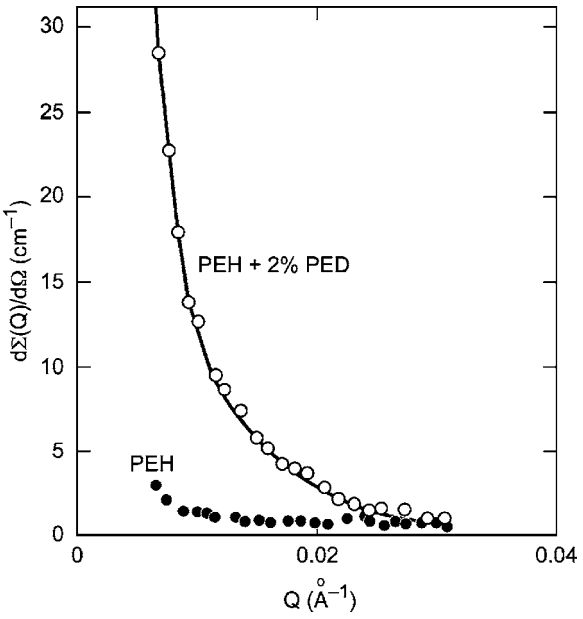

FIG. 2. $d\Sigma(Q)/d\Omega$ vs Q from H-polyethylene (blank) and 2% of D-polyethylene in the PEH matrix.

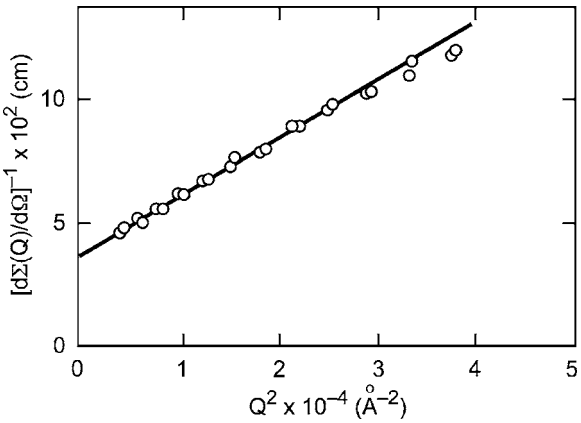

FIG. 3. Typical Zimm plot for 6 wt % D-polyethylene molecules in the H-polyethylene matrix quenched from the melt.

$$\left[\frac{d\Sigma(Q)}{d\Omega}\right]^{-1} = \left[\frac{d\Sigma(0)}{d\Omega}\right]^{-1}\left(1 + \frac{Q^2R_g^2}{3} + \cdots\right), \tag{7}$$

where $d\Sigma(0)/d\Omega$ is the value of the cross section at $Q=0$, and the R_g and M_w may be determined from the slope and intercept, respectively,[1] via

$$\frac{k_N c\rho^{-2}}{d\Sigma(0,c)/d\Omega} = \frac{1}{M_W} + 2A_2c, \tag{8}$$

where k_N is the contrast factor defined by Eq. (5),[1] c is the polymer concentration in g/cm^3, ρ is the polymer density, and A_2 is the second virial coefficient, which reflects the thermodynamic interactions between the components. As the "solute" and "solvent" consist of D^2- and H^1-labeled molecules of the same species, with the same chemical bonding, $A_2 \sim 0$, except at very high molecular weights ($M_w > 10^6$) where isotopic-induced critical scattering[33] or even phase demixing[34] can occur. Such effects are absent at modest molecular weights ($M_w \sim 10^5$), where the values determined by SANS and chromatography are in agreement within the experimental error.[32]

This study was conducted at low Q values to probe length scales of the order of the radius of gyration ($Q \sim R_g^{-1}$), and others were made on a range of amorphous polymers including poly(methyl methacrylate),[26] atactic polystyrene,[27–29] solid and molten polyethylene,[32] polyisobutylene,[35] polyethylene terepthalate,[36] a series of polymethyl methacrylates of different tacticities,[37] and polyethylene oxide.[38] This type of experiment measures the (z average) R_{gz} of the polymer chain, which may be converted to the weight-average radius (R_{gw}) if the polydispersity is known, and for monodisperse molecules, the two averages are the same. According to the Gaussian coil model,[23,24] R_g should be proportional to $M_w^{0.5}$, with the same constant of proportionality in the bulk as in an ideal Θ solvent, and the experiments show that in general this prediction holds well for amorphous polymers.[1]

While these results support this model, they are not in themselves conclusive since it was shown for crystalline polymers that R_g is very similar for molecules in the molten (amorphous) and solid (crystalline) states.[32] Thus, the finding that molecules exhibit the unperturbed dimensions in the molten or glassy amorphous state does not in itself prove that the configuration is Gaussian. In order to test how far the local molecular configuration, as opposed to the overall R_g, is described by the various models, measurements have been extended to higher values of Q. As explained above, the intensity at a given Q is sensitive to fluctuations in the scattering power on a distance scale $D \sim 2\pi/Q$, and thus as Q increases the scattering is increasingly determined by the local chain configuration. This may be calculated for the random coil model using rotational isomeric statistics,[24] and hence the scattered intensity may be estimated numerically and compared with experiment.

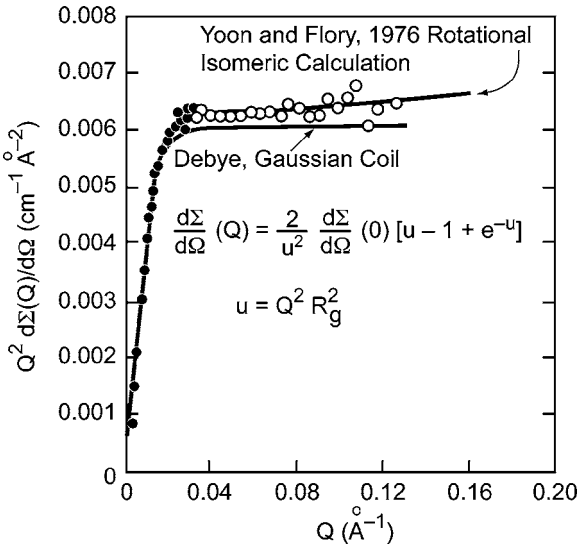

FIG. 4. Kratky plot for 6 wt % D-polyethylene molecules in the H-polyethylene matrix in the melt at 150 °C.

This is accomplished by measuring the scattering in the intermediate angle range ($0.1 < Q < 0.6$ Å^{-1}), which is sensitive to the local configuration of the chain over distances ~10–50 Å. Figure 4 shows intermediate angle neutron scattering (IANS) data for molten polyethylene[32] at $T = 150$ °C compared to the rotational isomeric state (RIS) calculation of Yoon and Flory[39] and the Debye model[3] for a coil with a Gaussian distribution of chain elements [Eq. (6)]. The data are plotted as $Q^2 d\Sigma/d\Omega$ vs Q as used by Kratky[15] since this representation enhances the scattering at higher Q and facilitates comparison with different models. It may be seen from Fig. 4 and Eq. (6) that $d\Sigma/d\Omega$ varies as Q^{-2} in this region, leading to a plateau in the Kratky plot, which is closely fitted by both the RIS calculation and the Gaussian coil function. Similarly, the IANS data for atactic polystyrene are consistent with the Debye model both in the melt and glassy states.[28,29] The RIS model reflects the local architecture (covalent bond lengths, interbond angles, etc.) of a particular chain,[31] and hence the agreement with the Debye function [Eq. (6)], which is based on general assumptions independent of the local chain architecture, is probably fortuitous. Thus, the Gaussian coil model has been very successful in predicting both the overall chain size and the local configuration in a range of amorphous polymers, and there are no major discrepancies between theory and experiment.

The successful application of the SANS method to elucidate the chain structure in the amorphous state has led to a wide application of the technique in materials science, in general, and in polymer science, in particular,[1,40,41] and in this review, we will describe some recent applications of the technique. The choice of the results included is, to some extent, personal, and an apology is made for the inevitable omission of significant research.

III. EXAMPLES OF SANS APPLICATIONS

A. Soft condensed matter

1. Wax crystal modification for fuel oils

Natural oil represents a complex mixture of normal alkanes which are described by the formula C_nH_{2n+2} and often designated simply as C_n. Oil can be separated into fractions via distillation, and at room temperature the first four alkanes are gases (C_1–C_4) and (C_5–C_{17}) are liquids with the distillation fractions (C_5–C_{11}), (C_9–C_{16}), and (C_{15}–C_{25}) corresponding to gasoline, kerosene, and diesel fuel, respectively. Hydrocarbons with ($C_{n\geqslant 20}$) are solids at ambient conditions and are usually called paraffins or waxes. Waxes are the major components of crude oils and diesel fuels, the presence of which is energetically desirable due to a higher combustion enthalpy with respect to the low-carbon alkanes. At the same time, the presence of waxes can cause significant technological problems due to their tendency to precipitate and form gels at low temperatures. The formation of a gel or large insoluble wax crystals can result in plugging pumps and transmission lines during the crude oil recovery from deep sea reservoirs, where there is a significant temperature drop between the reservoir and sea floor. Precipitation of large wax crystals from diesel fuels can clog engine filters and prevent operation under wintry conditions. Self-assembling polymers of various architectures have found commercial applications as additives acting as inhibitors in the wax precipitation and crystallization processes.[42] When mixed with oil, the polymers tend to aggregate at low temperatures. It has been known for a long time that the interplay between the polymer self-assembly and wax crystallization can be used to control wax gelation and thus make crude oils or diesel fuels flow at low temperatures. However, the exact mechanisms by which these additives influence the solubility and morphology of wax crystals was not completely understood, and the choice of additives for specific applications was often based on a trial and error practice rather than on solid scientific background.

Understanding the ways polymeric additives influence aggregation and gelation of waxes requires obtaining detailed structural information at different conditions such as temperature, fuel/oil composition, and concentration. Taking into account a mulicomponent nature of fuels and oils in addition to a variety of structures of the polymer additives, finding the regularities of the phase behavior of waxes may represent a challenging problem due to an almost unlimited number of the involved parameters. The problem may be simplified by investigating the behavior of model systems which mimic major properties of the complex multicomponent oils, and SANS can provide important information on the morphology of the formed aggregates due to its unique ability to manipulate the scattering length density of the constituent components. The cross section of a model oil (ternary system) consisting of a solvent (which can be chosen from one of the liquid alkanes C_5–C_{17}), a wax (an alkane with $C_{n\geqslant 20}$), and a polymer may be represented in terms of partial structure factors $S_{ij}(Q)$,[43]

$$\frac{d\Sigma(Q)}{d\Omega} = (\rho_p^* - \rho_s^*)^2 S_{pp}(Q) + 2(\rho_p^* - \rho_s^*)(\rho_w^* - \rho_s^*) S_{pw} + (\rho_w^* - \rho_s^*)^2 S_{ww}(Q), \tag{9}$$

where subscripts "p," "w," and "s" indicate polymer, wax, and solvent, respectively. The prefactors $\Delta\rho_{i,j}^* = (\rho_i^* - \rho_j^*)$ are proportional to the neutron contrast between the i_{th} and j_{th} components (see Sec. II A). Using a mixed (H+D) solvent, with the neutron SLD matching that of the polymer or the wax (see Table I), one can annul either the first and second or the second and third terms in the right-hand side of Eq. (6) and thus make only the wax or the polymer component visible for neutrons.

At high temperatures polymer additives and waxes are soluble in liquid alkanes and SANS can provide information on the conformation and thermodynamic properties of the individual solutes. As the temperature is decreased, the polymer and the wax may form aggregates, the scattering from which is often characterized by the power law,[40]

$$\frac{d\Sigma(Q)}{d\Omega} \sim Q^{-\alpha}, \tag{10}$$

where the exponent α characterizes a specific structure of the scattering object and can provide immediate semiquantative insight in the morphology of the self-assembled aggregates. For instance, for scattering from a single polymer chain swollen in a good solvent, $\alpha = 5/3$ and $\alpha = 2$ for the "unperturbed" polymers in the Θ condition. Scatterings from more compact structures such as one-dimensional rods or two-dimensional platelets are described by $\alpha = 1$ and $\alpha = 2$, respectively. Exponents of $\alpha < 3$ and $3 < \alpha < 4$ correspond to the mass and surface fractals, respectively, whereas $\alpha = 4$ describes scattering from three-dimensional objects with sharp interfaces. In combination with the contrast matching technique, Eq. (10) can be used to analyze specifics of the structure of the aggregate core or the polymer conformation in the surrounding polymer brushes depending on which part of the aggregate is made visible by choosing an appropriate neutron contrast.

Studies of the self-assembling behavior of potential wax crystal modifiers based on poly(co-olefins) were initiated by the Exxon-Infineum Corporation in the late 1990s, and SANS was first applied to study the aggregation in the wax-free *binary* solutions of semicrystalline diblock and random copolymers in decane (C_{10}). At high temperatures ($T \geqslant 70\,^\circ\text{C}$) polyethylene-poly(ethylene propylene) (PE-PEP) diblock copolymers as well as poly(ethylene-butane) (PEB) random copolymers form homogeneous solutions in decane. As the temperature is decreased, the polyethylene component of these copolymers may crystallize, which provides the thermodynamic reason for aggregation. The structure of ag-

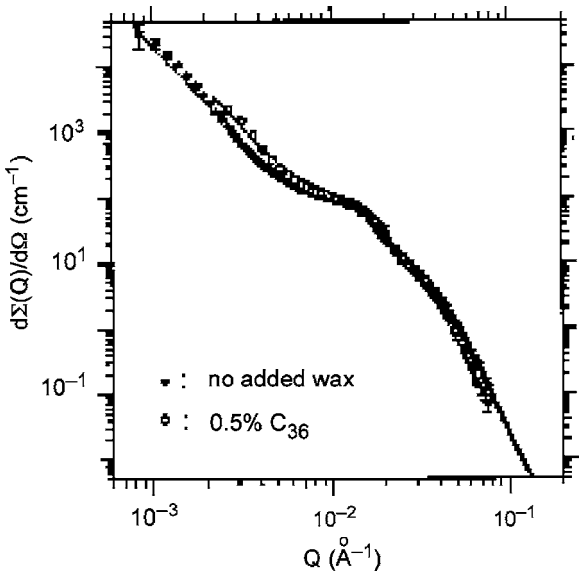

FIG. 5. $d\Sigma(Q)/d\Omega$ vs Q from polyethylene-poly(ethylene-propylene) (PE-PEP) diblock copolymer (M_W=6000/10 000, ϕ=2%) in decane under the "core contrast" with and without the addition of 0.5% C_{36}. The SLD of the wax is equal to that of the solvent which makes the wax "invisible" to neutrons (Ref. 49).

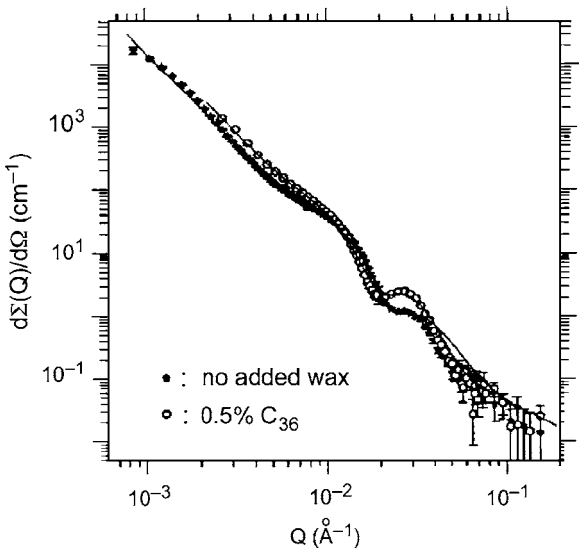

FIG. 6. $d\Sigma(Q)/d\Omega$ for the same system as in Fig. 5, but under the "brush contrast." SLDs of the core and wax are matched to that of solvent, which makes them invisible to neutrons. These data make it possible to reconstruct the brush concentration profile with and without added wax (Ref. 49).

gregates formed by PE-PEP diblock copolymers, with the molecular weight of each block varied in the range 5000–16 000, was evaluated using SANS.[44,45] A detailed analysis has led to a structural model, where the diblocks form crystalline PE platelets with a thickness in the range between 20 and 100 Å surrounded on both sides by a PEP polymer brush with a characteristic size of the hairs of the order of 200 Å. A rather different behavior was revealed in solutions of PEB random copolymers where crystallizable and amorphous blocks are randomly distributed along the chain. A formation of long rodlike structures was observed[46] in solutions of PEB-11 copolymer (11 is the number of ethyl groups per 100 carbons in the backbone of the chain). The specifics of the PEB aggregate morphology were explained by cocrystallization of the PE microcrystallites hindered by the amorphous segments of the polymer. The results of these studies suggested that semicrystalline copolymers may control the formation of large wax crystals and gels by nucleating numerous smaller crystals on the copolymer microcrystallite structures covered with amorphous "hairs" or "brushes," which work as steric barriers preventing further aggregation and thus help to keep the platelets in solution.[47,48]

The first study of the model oils (ternary wax-containing solutions) was conducted by Leube *et al.*,[49] who used SANS to investigate the influence of PE-PEP diblock copolymers on the crystallization of C_{30} and C_{36} waxes in decane. Two different approaches were chosen to study the morphology of the polymer-wax aggregates. In the first set of experiments the change in the platelet structure in the presence of wax was investigated. For this purpose, the solutions were prepared at the conditions at which the neutron scattering length density of the wax and the brush were matched with the solvent by choosing an appropriate composition of the mixed (H+D) wax and (H+D) solvent. Figure 5 shows the SANS data from a PE-PEP block copolymer in a mixed solvent (0.946 $C_{10}D_{22}$+0.054 $C_{10}H_{22}$) with a mixture of hydrogenated and deuterated wax (0.5 $C_{36}D_{74}$+0.5 $C_{36}H_{74}$), which makes only the PE core visible to neutrons. As shown in Fig. 5, in the range of scattering vectors $Q > 8\times10^{-3}$ Å^{-1}, which is relevant to the scattering from the PE core, the cross section from the solution with and without wax is the same, indicating that cocrystallization of the wax and PE does not occur. Figure 6 shows the SANS data from the same sample taken under different neutron contrast conditions. Here, the composition of the (D+H) wax is the same as before. However, the ratio of D- and H-decane is different (0.025 $C_{10}D_{22}$+0.975 $C_{10}H_{22}$) and matches the scattering length density of the core and thus makes only the structure of the polymer brush visible. As may be seen in Fig. 6, the scattering from a brush is modified in the presence of a wax: the dip around $Q\sim2\times10^{-2}$ Å^{-1} is shifted to smaller Q values and the hump at $Q\sim3\times10^{-2}$ Å^{-1} becomes more pronounced, indicating the formation of a much sharper concentration profile of the brush. The quantitative analysis of the conformation of an amorphous polymer was performed by fitting the cross section to the form factor of a polymer brush, which showed that the polymers are stretched at the aggregate surface due to precipitation of the wax on the surface of PE platelets.

Experiments were continued to study the efficiency of other polymer additive architectures, and Schwahn *et al.*[43] used SANS to explore the influence of PEB random copolymers on crystallization of the C_{24} wax in decane at different wax concentrations and temperatures. A structural evaluation of the aggregates has shown that, contrary to the wax-free solutions where PEB crystallizes to form one-dimensional structures, in the presence of wax PEB cocrystallizes with the paraffin in thin platelets surrounded by the amorphous polymer hairs or loops. These platelets are capable of nucleating small three-dimensional wax crystals whose growth is hindered by the presence of the polymer. The investigations

were continued by Ashbaugh *et al.*,[47,48] and Radulescu *et al.*[50–52] who used SANS along with rheology to study the influence of the structure and molecular weight of PEB copolymers on the crystallization of C_{24} and C_{36} waxes. The yield stress of the untreated model oil was measured to be in the range of 250–500 Pa. However, adding only 500 ppm of PEB decreased the yield stress of the wax gel by three to four orders of magnitude. Parallel structural SANS experiments demonstrated that the wax crystal modification is highly sensitive to the ethylene content of the backbone as well as the molecular weight of the polymer, and these parameters can be used for tuning the wax aggregation.

The above examples demonstrate the power of SANS to characterize rich morphologies which can form in crude oils and middle-distillate fuels at different conditions. The technique of contrast variation and matching is essential for a structural characterization of complex systems and measurements at a single contrast, e.g., in x-ray or light scattering experiment, would be insufficient to get accurate information on the structure and morphology of individual components. Systematic structural SANS studies of PE-PEP—induced wax crystal modification in model oils—have helped to delineate some of the fundamental processes which control the formation of wax gels and large aggregates. This information was used in part for the formulation of the diesel fuel additive Paraflow™ based on these diblock copolymers. The results of extensive SANS studies of the structure of PEB random copolymers have also demonstrated their potential as flow improvers for waxy crude oils and petrochemical products.

2. Aqueous microemulsions in supercritical carbon dioxide

Liquid or supercritical carbon dioxide (CO_2) is a promising solvent for material synthesis and processing, though it has an important limitation, namely, its low capacity for solubilizing many materials, including water. One way this issue has been addressed is through the use of small-molecule surfactants to aid the dispersion of water-in-CO_2 (W/C) via the formation of W/C microemulsions. With the assistance of grafted copolymers[53] or specially designed surfactants,[54–56] stable and transparent microemulsion systems that can disperse water and other solutes have been achieved.

Most of the surfactants that form W/C microemulsions are anionic and have fluorocarbon tails that are easily solvated by CO_2,[57,58] such as the fluorinated analog of Aerosol-OT (AOT),[59] ammonium carboxylate perfluoropolyether ($PFPECOO^-NH_4^+$),[54] and phosphorous fluorosurfactants.[55,60] The W/C microemulsion systems formed with $PFPECOO^-NH_4^+$ have been intensively studied by means of SANS, SAXS, NMR, and other techniques.[54,61–67] In order to illustrate the utility of small-angle scattering techniques, particularly SANS, in characterizing such systems, we will focus our attention on phosphorous fluorosurfactants of bis-[2-(F-hexyl)ethyl] phosphate salts. SANS and NMR were used to determine the conditions under which microemulsions form, the structure of the microemulsion droplets, their capacity for solvating water, the mobility of entrapped water,

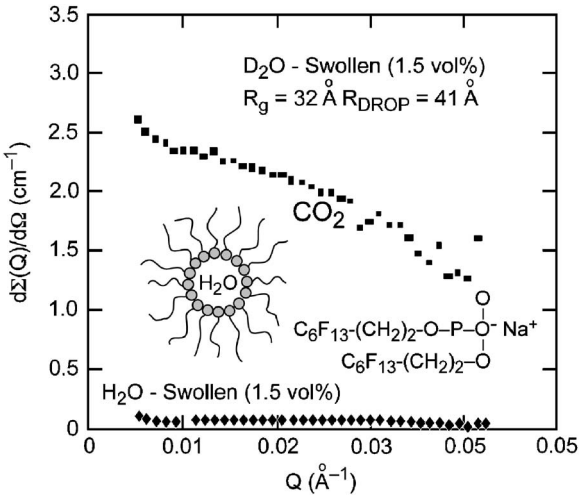

FIG. 7. Schematic illustration of microemulsion structure and SANS cross section for phosphate ester surfactants swollen with H_2O and D_2O.

and droplet diffusion coefficients as a function of density.[68] Figure 7 shows a schematic of the microemulsion structure, where water molecules are entrapped inside the droplets and are also present at low concentrations in the CO_2 continuous phase. A shell region composed of surfactant tails and some associated CO_2 exists between the head groups in the droplets and the CO_2 continuous phase. SANS is sensitive to the water droplet (core) dimensions and provided an estimate of their size and the variation with pressure and temperature. Complementary NMR diffusion measurements provided a hydrodynamic radius that was similar to the SANS dimensions.[68]

SANS experiments were conducted in a cell that has been used extensively for previous neutron scattering experiments.[55,56,69] Due to the high penetrating power of neutrons, the beam passed through two ~1 cm thick sapphire windows with virtually no parasitic scattering or attenuation (cell transmission ~93%). The "background" scattering from the gaseous medium represented a small perturbation, typically of the order of 0.04 cm^{-1}, and was subtracted from the "sample" data with the same CO_2 pressure.

The contrast, which is necessary in a SANS experiment in order to render information about the structure, is provided by the difference between the SLD or neutron refractive index of the microemulsion droplets, on the one hand, and that of the solvent, on the other. As pointed out by Eastoe *et al.*,[70] the SLD of D_2O ($\sim 6.4\times10^{10}$ cm^{-2}) is much higher than the SLDs of CO_2 (see Table I) or the surfactants, both of which are $\sim 2\times10^{-2}$ cm^{-2}. Thus, the SLDs of the surfactant shell (ρ_2^*) and CO_2 solvent are essentially matched ($\rho_{CO_2}^* \cong \rho_2^*$), and the scattering comes principally from the contrast between the D_2O core and CO_2. This is illustrated in Fig. 7, which shows the cross sections for solutions of 7.5 wt % phosphate ester surfactants, swollen with D_2O and H_2O at 173 bars after subtracting the CO_2 background. It may be seen that the signal (~ 0.06 cm^{-1}) from the H_2O-swollen material is of the same order as the incoherent background and well over an order of magnitude less than that of the D_2O-swollen solution $[d\Sigma(0)/d\Omega \sim 3$ $cm^{-1}]$.

Thus, the majority of the scattering comes from the deuterium-labeled nanodroplets, which form the core of the microemulsions.

For low microemulsion concentrations, particle interactions may be neglected to first order, and the scattering from individual particles may be approximated by $d\Sigma(Q)/d\Omega \cong d\Sigma(0)/d\Omega \exp[-(QR_g)^2/3]$. Thus, typical Guinier plots of $\ln[d\Sigma(Q)/d\Omega]$ vs Q^2 are linear,[71] with slope $(R_g^2/3)$, and the corresponding core radii are given by $R_1=(5/3)^{0.5}\ R_g$. For higher concentration microemulsions, the analysis may be extended to allow for interparticle interactions between the droplets and for polydispersity effects.

Following the formalism employed by Steytler *et al.*,[60] Eastoe *et al.*,[66,70] and Lee *et al.*,[64,65] the solutions were represented as a collection of polydisperse particles, assuming no orientational correlations, and the coherent differential scattering cross section is given by

$$\frac{d\Sigma(Q)}{d\Omega} = N_p\{\langle|F(Q)|^2\rangle + |\langle F(Q)\rangle|^2[S(Q)-1]\} + B, \quad (11)$$

where N_p is the number density of particles, $F(Q)$ is the particle form factor, $S(Q)$ is the structure factor arising from interparticle scattering, and B is the background from CO_2 ($\sim$0.04 cm^{-1}), previously subtracted. Spherical particles with a centrosymmetric distribution of scattering length density may be modeled by concentric shells,[72,73] and for a core/shell micelle the intraparticle term in Eq. (11) may be expressed as

$$\langle|F(Q)|^2\rangle = \int |F(Q,R_1)|^2 f(R_1)dR_1, \quad (12)$$

where R_1 is the radius of a core, which occurs within the distribution of core radii with a normalized frequency of $f(R_1)$. The form factor of a particle with a core radius R_1 and an outer radius R_2 is given by

$$F(Q,R) = \frac{4\pi}{3}[R_1^3(\rho_1^* - \rho_2^*)F_0(QR_1) + R_2^3(\rho_2^* - \rho_3^*)F_0(QR_2)]$$

$$F_0(x) = \frac{3}{x^3}(\sin x - x\cos x), \quad (13)$$

where ρ_1^*, ρ_2^*, and ρ_s^* are the SLDs of the core, shell, and solvent, respectively.

Several particle shapes have been used to calculate the intraparticle term (or form factor). In general, for micelles in CO_2, the best fits have been given by a spherical core-shell model with a Schultz distribution[60,70,72,73] of particle sizes,

$$f(R_1) = \frac{(Z+1)^{Z+1}X^Z \exp[-(Z+1)X]}{\overline{R_1}\Gamma(Z+1)},$$

$$Z = \frac{1-(\sigma/\overline{R_1})^2}{(\sigma/\overline{R_1})^2},$$

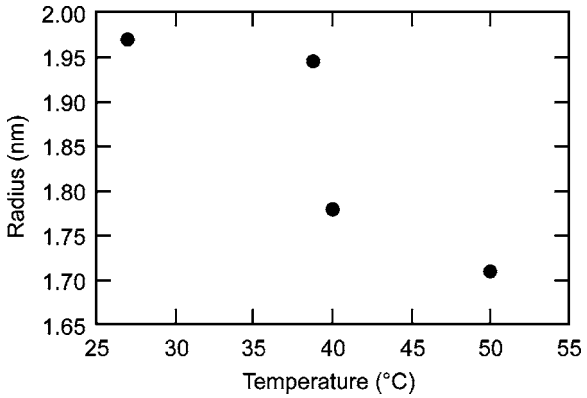

FIG. 8. Temperature dependence of water droplet dimensions.

$$X = \frac{R_1}{\overline{R_2}}, \quad (14)$$

where σ^2 is the variance of the distribution and Z is the breadth parameter. $S(Q)$ was modeled[60,64–66,70] via an attractive Ornstein-Zernike structure factor, characterized by a correlation length ξ and $S(0)$,

$$S(Q) = 1 + \frac{S(0)}{(1+Q^2\xi^2)}. \quad (15)$$

Equation (15) has been widely used[60,66,70] to account for interactions for surfactant concentrations $\sim$0.05 mol dm^{-3} and for values of W_0 (the mole ratio of water to surfactant) in the range $4<W_0<20$, where $S(Q)$ departed from unity only for high values ($W_0>30$). Allowance for particle polydispersity [via Eq. (13)] resulted in values of the Schultz breadth parameter in the range $8<Z<16$ for phosphorous fluorosurfactant microemulsions, and similar polydispersity parameters have been observed[60,70] for other micelles formed by fluorosurfactants in CO_2. For systems with the values of W_0 around 7 and D_2O content up to 3.2 vol %, $S(0)$ was also allowed to "float," along with the correlation length ξ. The latter generally gave values typically 70–100 Å, and the analysis was found to be insensitive to ξ in this range, as previously observed.[60,70] Fitting R_1, $S(0)$, and ξ, or fitting R_1 and $S(0)$ with fixed $\xi\sim$100 Å, generally gave values in the range $-0.1<S(0)<0.1$, confirming that the effect of interactions was small. Thus, the allowance for interactions generally changed R_1 by less than 3%, which is less than the overall uncertainty in R_1 (±2 Å) generally expected from a SANS analysis for similar systems.

As discussed previously, the SLDs of the surfactant shell and CO_2 solvent are essentially matched ($\rho_{CO_2}^* \cong \rho_2^*$), so the scattering comes principally from the contrast between the D_2O core and CO_2. Thus, the water pools can be sized in terms of a core radius R_1. Figure 8 shows that for a surfactant concentration of 0.027 mol dm^{-3} and an initial pressure of 140.9 bars, the core radius R_1 falls by 13% as the temperature is raised from 26 to 50 °C. An increase in temperature in this range affects the core radius even less (3%–4% decrease) for a surfactant concentration of 0.015 and 0.054 mol dm^{-3}. Figure 9 shows that at the same temperature (27 °C) for fixed amounts of loaded water (W_0 around 5) and

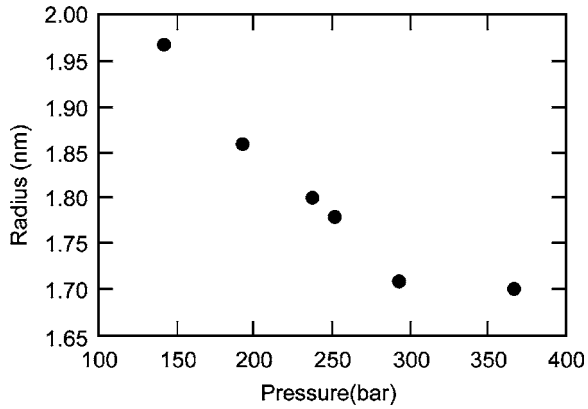

FIG. 9. Pressure dependence of water droplet dimensions.

surfactant (0.027 mol dm^{-3}), R_1 falls by around 14% as the pressure increases from 171.8 to 378.0 bars, and these trends are consistent with the results of Eastoe *et al.*[70]

NMR can provide a complementary estimate of the micelle dimensions. Under conditions corresponding to 25 °C, 206.1 bars, $W_0=5$, and a surfactant concentration of 2.5 wt %, the diffusion coefficient for the surfactant tails ($-CH_2CH_2O-$), combined with the Stoke-Einstein equation, yields a hydrodynamic radius of $R_h=20$ Å. For the same conditions, SANS gives $R_1=18.5$ Å, which gives $R_g=(3/5)^{0.5}R_1=14.5$ Å and $R_h=18.7$ Å, assuming the theoretical ratio of $R_g/R_h=0.775$ for a solid sphere.[74] The agreement is reasonable in view of the fact that the SANS and NMR techniques are weighted to measure somewhat different parts of the structure. Thus, as discussed above, the SLD contrast between the shell and the CO_2 medium is small, so the scattering comes principally from the contrast between the D_2O core and CO_2 and therefore monitors the size of the water pools in the *core* of the micelle. The NMR signal, however, arises from the surfactant tails, which are preferentially located in the *shell* of the system[68] and would therefore be expected to be sensitive to somewhat larger dimensions (see Fig. 7), as would be the case for SANS if the tails were *deuterated*. Thus, SANS confirms the slight swelling of the micelles as W_0 is increased, and has quantified the fall in the core radii (R_1) as the temperature is raised for different surfactant concentrations. In addition, for fixed W_0 and temperature, R_1 is inversely proportional to the pressure, and there is a reasonable agreement between the micelle dimensions as measured by NMR and SANS.

As mentioned above, other surfactants that have been shown to be capable of forming W/C microemulsions include cationic perfluoroether trimethylammonium acetates over a range of temperatures (25–90 °C) and pressures (87–415 bars). SANS studies by Lee *et al.*[64] were interpreted in terms of spherical droplets with radii ranging from 16–36 Å for W_0 ratios of 9–28. The SANS data indicated a smaller area (60–72 $Å^2$/surfactant molecule) at the water-CO_2 interface than for anionic perfluoroether surfactants, which was attributed to the CO_2-phobic functionality between the surfactant head group and the perfluoroether tail, which reduces CO_2 penetration of the tails.

Other SANS investigations of water-in-CO_2 microemulsions were undertaken by Eastoe *et al.*,[66] who developed much of the SANS methodology described above. W/C microemulsions formed by dichain hydrocarbon-fluorocarbon surfactants were investigated via SANS, which was interpreted in terms of spherical droplets and modeled as a system of core-shell particles obeying a Schultz distribution of radii [Eqs. (11)–(14)]. The average core radius was ~25 Å, and the molar ratio of water/surfactant was W_0 ~33. As in the above examples, the SANS signal was maximized by using D_2O to swell the micelle. Similarly, Zielinski *et al.*[75] studied D_2O-swollen microemulsions of ammonium perfluoropolyether surfactants. As the D_2O concentration increased, the core radius increased from 20 to 35 Å, and at constant water concentration the micellar structure was essentially independent of pressure. In both studies, the surfactant was shown to dissolve up to its own weight (~2%) of water in CO_2, and the critical fluctuations increased as the pressure was reduced and the phase boundary was approached.

In addition, novel sodium salts of bis(octafluoro-1-pentyl)-2-sulfosuccinate[76] have also been shown to be among the family of small molecules capable of stabilizing W/C microemulsions under a range of conditions (up to 60 °C and 350 bars). In this example, the presence of microemulsions was confirmed by SAXS. An analysis via the core-shell model, however, gave core radii that were essentially constant as the shell radius increased with increasing W_0. This result was believed to be unphysical. The data were therefore modeled as monodisperse cylinders, and the median cylinder radius (r) were observed to grow approximately according to $r \sim W_0$ in the range $8<r<30$ Å, while the cylinder length (L) was observed to grow approximately according to $L \sim W_0^2$ in the range $50<L<240$ Å. Typical water loadings range up to ~10 vol % for this class of surfactants, and this is the highest water concentration achieved for W/C microemulsion systems at comparable pressures and temperatures,[76] representing an increase of well over an order of magnitude higher than the natural solubility of water in CO_2.

As indicated above, neutron scattering may be applied to characterize CO_2-soluble molecules and is particularly suited to study the structure of fluids under pressure due to the high transmission of many of the materials used in the construction of pressure vessels. Mathematical modeling of the data in terms of core-shell micelle structures, with water solubilized in the cores, permits a detailed description of the structure. As mentioned above, this methodology has been extensively used to model SANS from micelles in aqueous media[9–11,77] and blockcopolymer micelles in CO_2.[72,78,79]

These studies reflect the growing interest in CO_2-soluble amphiphiles to provide havens for hydrophilic materials in CO_2 and thus broaden the potential applications in separations and extraction processes. The use of such highly CO_2-soluble amphiphiles may allow the operating pressure of novel extraction processes to be lowered closer to the point of economic viability. In addition, CO_2-soluble dendritic molecules have been shown[80] to act as micellelike entities, which are capable of solubilizing CO_2-insoluble mate-

rials (e.g., polar ionic species) in their cores. Such materials are finding applications in cleaning processes.

Similarly, many polymers, waxes, etc., that do not dissolve in CO_2 may be solubilized by means of diblock copolymer surfactants consisting of "CO_2-phobic" and "CO_2-philic" blocks.[72,78,79] Understanding the solubility mechanisms that enable polymers to be dissolved and processed in supercritical CO_2 is important in the development of more environmentally benign technologies, and new industrial processes, facilitated by the insights provided by SANS, are being developed.[81] SANS research on polymer blends, in particular, and on soft matter, in general, have many practical applications.[1] So much of the research on these materials has links to industrial R&D, and introductory reviews have been given by Lohse,[2] Sinha *et al.*,[3] and Lindner and Wignall.[82]

3. Block copolymers as efficiency boosters for water-oil microemulsions

SANS can also give similar detailed information on the structure and interactions in oil-in-water microemulsions as in the W/C systems described above. A particularly good example is the structural insight provided by neutron scattering into the recently discovered effect of the dramatic enhancement of the water-in-oil (W/O) solubility in ternary water-oil-surfactant microemulsions by block copolymers. Such surfactants are generally amphiphilic (i.e., the different components of the molecule have different solubilities), and it is well known that hydrophobic oil may be solubilized in water by coating the oil droplets with the hydrophilic (water-soluble) component of a detergent. Because aggregates formed by surfactants in a predominantly water phase have been traditionally referred to as "normal" micelles, those forming in a predominantly oil matrix are often referred to as "reverse micelles" or "inverted micelles."[78] Similarly, aggregates that form in CO_2 may also be referred to as reverse micelles, as the hydrophilic component is in the core, and those that are capable of absorbing appreciable amounts of water are described as water-in-CO_2 microemulsions by analogy with water-in-oil systems.

Microemulsions are of growing interest both in industry and research, and for both commercial and environmental reasons, it is desirable to form such solutions using as little surfactant as possible. Starting from the well-known phase behavior of a ternary microemulsion system with water, *n*-decane, and *n*-decyl-tetraoxyethylene ($C_{10}E_4$), Jakobs *et al.*[83] observed that the amount of surfactant needed to form a thermodynamically stable, homogenous mixture could be significantly reduced by the addition of a block copolymer (PEP_x-PEO_y). Alternatively, the "efficiency" of the surfactant to form microemulsions could be "boosted," and the solubilization capacity increased by such amphiphilic additives. In microemulsions, the surfactants form a flexible interfacial film separating the two incompatible oil and water species into subphases.

This process is illustrated in Fig. 10, which shows a sample containing equal volumes of water and *n*-decane ($\phi=0.5$) and a surfactant weight fraction $\gamma=0.030$ separated into three phases, the middle phase (microemulsion) taking

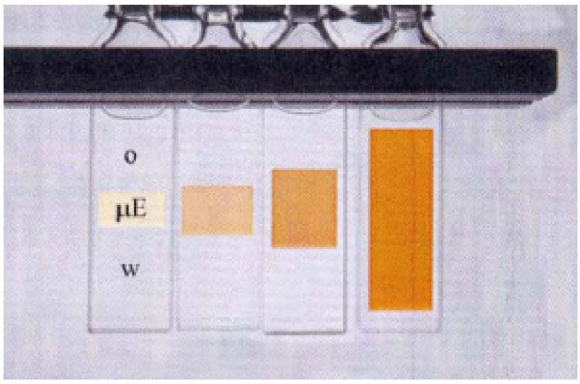

FIG. 10. (Color online) Samples of H_2O-*n*-decane-$C_{10}E_4$ in Hellma quartz cells at 30.3 °C. From left to right the concentration of the PEP_5-PEO_5 block copolymer increases: (a) 0%, (b) 1.5%, (c) 5%, and (d) 11.5%, leading to a dramatic increase of the volume of the middle phase.

up about $\frac{1}{4}$ of the phase volume, as indicated in the leftmost cell. After adding PEP_5-PEO_5, the volume fraction of the middle phase increases dramatically, as shown in the other three samples with mass fractions of the block copolymer in the surfactant/copolymer mixture of 1.5%, 5%, and 11.5%. Thus, the oil and water excess phases visible in the left test tubes are progressively swallowed by the surfactant-rich middle phase, as it increases in volume. The accompanying effect of increasing opalescence leads to an increasingly darker appearance of the middle phases in transmitted light, which is related to the increasing length scale, leading to stronger (light) scattering.

As discussed above, the scattering signal arises from differences or fluctuations in the SLDs (ρ_i^*) of the components, and for a bicontinous micremulsion (representing a quaternary system) the cross section may be expressed as[84]

$$\frac{d\Sigma(Q)}{d\Omega} = (\rho_o^* - \rho_w^*)^2 S_{oo}(Q) + (\rho_f^* - \rho_w^*)^2 S_{ff} + (\rho_p^* - \rho_w^*)^2 S_{pp}(Q) + 2(\rho_o^* - \rho_w^*)(\rho_f^* - \rho_w^*) S_{of} + 2(\rho_f^* - \rho_w^*)(\rho_p^* - \rho_w^*) S_{fp}(Q) + 2(\rho_o^* - \rho_w^*)(\rho_p^* - \rho_w^*) S_{op}(Q), \quad (16)$$

where the subscripts *o*, *w*, *f*, and *p* indicate oil, water, film, and polymer, respectively, and $S_{ij}(Q)$ are the partial structure factors,[85] which reflect the contributions of the various components of the microemulsions. It may be shown that for $\rho_f^*=\rho_w^*$, the cross section is proportional to $S_{oo}(Q)$ and therefore contains information on the structure of the "bulk" phase. Similarly, for $\rho_o^*=\rho_w^*$, the signal reflects $S_{ff}(Q)$ and therefore reveals information about the surfactant correlations in the "film." For $\rho_o^*=\rho_w^*=\rho_f^*$, the signal is dominated by the polymer-polymer structure factor $S_{pp}(Q)$ and provides information about the structure of the polymer.

Despite the apparent complexity of the scattering indicated in Eq. (16), the ability to match the SLDs of different components by mixing both protonated (H-labeled) and deuterated (D-labeled) components (e.g., H/D decane, H/D surfactants, H_2O/D_2O) and therefore remove one or more of the components from the scattering allows the various structural contributions to be isolated.[84] Thus, isolating the bulk scat-

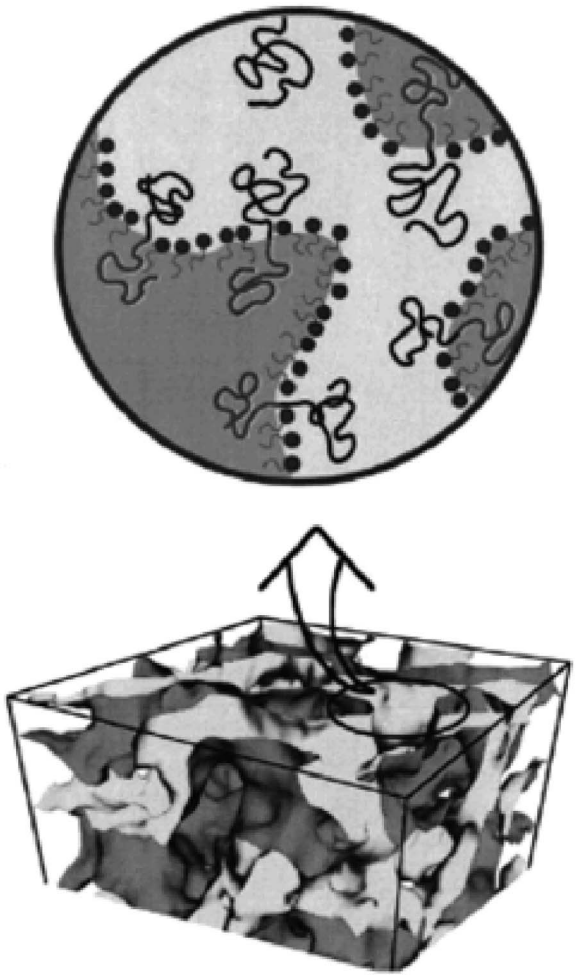

FIG. 11. Schematic illustration of the bicontinulus microemulsion structure and the polymer distribution on the interface as inferred from the SANS data described in this paper.

tering directly gives the specific surface per unit volume in addition to the interface roughness. Similarly, determining the film scattering function allows a close comparison with theoretical models based on the Ginzburg-Landau-type free-energy functional approaches,[85,86] as well as Gaussian-random-field models.[87–89] Finally, the most difficult information to extract is the evaluation of the "polymer" scattering arising from a material that occupies <1 vol %. It therefore requires very careful subtractions to isolate this component.[84]

In summary, the analysis of the partial structure factors provides detailed information on the structure of the microemulsions and the conformation of the polymers and their location relative to the surfactant film. It was shown that the scattering data were consistent with polymer coils, which behave as self-avoiding chains anchored to a virtually planar surface. These were uniformly distributed as single coils and did not aggregate to form block copolymer micelles. A schematic illustration of the bicontinuous microemulsion structure inferred from the SANS results is shown in Fig. 11.

This research area belongs to one of the most rapidly developing fields of soft matter, which encompasses a variety of increasingly complex systems being used as the building blocks for new materials and technologies. Water-in-oil microemulsions represent an important example of soft materials, which manifests a strong response to relatively weak perturbations. Thus, adding only a small fraction (<1 vol %) of amphiphilic block copolymer induces a spectacular (>200 vol %) increase in the volumes of water and oil solubilized into a bicontinuous microemulsion. Moreover, the enhanced turbidity exhibited by the system indicates a structural rearrangement which extends over two orders of magnitude from the original dimensions observed by neutron scattering (~ 100 Å) to a size range which scatters light ($\sim 10\,000$ Å). This effect represents yet another fascinating aspect of soft matter: the fact that an additive, in very small quantities, can change virtually everything in the system. Due to its relevance to a numerous basic and technological problems, understanding the underlying mechanisms of "efficiency boosting" is of both fundamental and practical importance.

The systematic studies performed have shown that the efficiency boosting is a universal phenomenon, which occurs in a wide range of the molecular weight of the block copolymer. SANS experiments combined with exceptionally delicate two-dimensional contrast variation techniques[90] have demonstrated that the enhancement of the swelling behavior is due to the variation of the membrane elasticity by polymer "mushrooms" uniformly distributed over the interface. Detailed theoretical calculations of bending energy have disclosed the mechanism of the efficiency boosting to be due to the variation of the surfactant film curvature elasticity by tethered polymers. A predicted fluctuation-induced decrease of the membrane bending rigidity as well as the exponential variation of optimal composition with the polymer concentration were successfully confirmed by the neutron experiments.

B. Hard nanostructured materials

1. Structure of low-dielectric constant films

The demand for increased signal transmission speed and device density in the next generation of multilevel integrated circuits requires the use of low-dielectric constant (low-k) materials with permittivities of less than 2.0. The lowered dielectric constant has the effect of increasing signal propagation speed, decreasing the energy needed to propagate a signal and decreasing the cross-talk between adjacent conductors. One avenue to low-k materials is the introduction of nanometer size pores into a solid film to lower its effective dielectric constant. For example, the dielectric constant of bulk silica, nominally about 4, reduces down to 2 if the film porosity approaches three-quarters by volume.[91] At the same time, the introduction of voids may affect important material properties such as mechanical strength, moisture uptake, coefficient of thermal expansion, and adhesion to different substrates. The characterization of the pore structure is needed by materials engineers to help optimize and develop future low-k materials. Therefore, there is a strong need for high quality structural data to help understand correlations between processing conditions and the resulting physical properties.

SANS contrast variation or contrast matching is an established method of characterization of the matrix structure

and closed pore content in bulk nanoporous materials.[92] In a contrast variation experiment, pores are filled with liquid solvents of variable neutron SLD (e.g., mixtures of D_2O and H_2O of different compositions). Neutron scattering intensity depends on the neutron contrast proportional to the difference between the SLD of the solvent and that of the matrix. The solvent SLD is varied systematically, and the scattered intensity is measured at each composition. In materials with a homogeneous atomic composition and absent closed (i.e., inaccessible to the solvent) pores, the contrast variation can be used to measure the physical density of the matrix. If the contrast matching point cannot be reached, information can be obtained about the concentration and size of the closed pores, which are responsible for the nonzero coherent scattering from the sample in the contrast matching point for a chemically homogeneous matrix of the porous material.

The first attempt to apply SANS for a structural characterization of porous *thin films* with the thickness of the order of 1 μm was undertaken by Wu *et al.*[93] who evaluated the structural properties of porous silica (xerogel) thin films supported on silicon wafer substrates. To enhance the scattering signal, the samples were composed of a stack of six pieces of the wafer with the thin film. Since the silicon wafer substrate supporting the porous film is virtually transparent to neutrons and does not cause significant scattering in the small-angle region, the measured scattering intensities are exclusively from the porous films due to neutron contrast between the SLD of the pore walls and the SLD of pores themselves which can be taken as zero. The neutron contrast was varied by preparing three different samples, one with pores saturated with air to evaluate the film structure, one with pores saturated with deuterated toluene to determine the pore connectivity, and one with pores saturated with deuterated water to measure moisture uptake. A suitable model to describe the film structure is a random two-phase model by Debye-Anderson-Brumberger (DAB),[94]

$$\frac{1}{[d\Sigma(Q)/dQ]^{1/2}} = \frac{1}{(c\xi^3)^{1/2}} + \frac{\xi^2 Q^2}{(c\xi^3)^{1/2}}, \tag{17}$$

where ξ is a correlation length (i.e., a composite phase size for the material including both pore and matrix phases), which is related to the average dimension or the chord length, of the pores l_C and the volume fraction of pores ϕ_0 as $\xi = l_C(1-\phi_0)$, c is defined as $8\pi\phi_0(1-\phi_0)(\Delta\rho^*)^2$, and $\Delta\rho^*$ is the difference between the SLD of the pore walls and pores, the latter taken to be zero for empty (i.e., air filled) pores. The values of c and ξ can be determined from the slope and intercept of the SANS data plotted as $[d\Sigma(Q)/d\Omega]^{1/2}$ vs Q^2 in the intermediate Q range $Q^2 > 0.0002$ Å^2 (see Fig. 12). The slope and the $Q=0$ intercept in the Fig. 12 are 163.2 ± 0.9 cm$^{1/2}$ Å^2 and 0.175 ± 0.002 cm$^{1/2}$, respectively. For the mass density of the sample 0.55 g/cm^3 and the density of the wall material 1.16 g/cm^3, this gives the porosity $53\% \pm 1\%$ and a pore chord length of 65 ± 1 Å. The deviation (downturn) from the linear dependence $[d\Sigma(Q)/d\Omega]^{1/2}$ vs Q^2 at small Q, often referred to as "excess forward scattering," is observed in many porous materials and is believed to occur due to a nonuniform distribution of pores (e.g., clustering of pores) or the presence of large scale chemical heterogeneities.

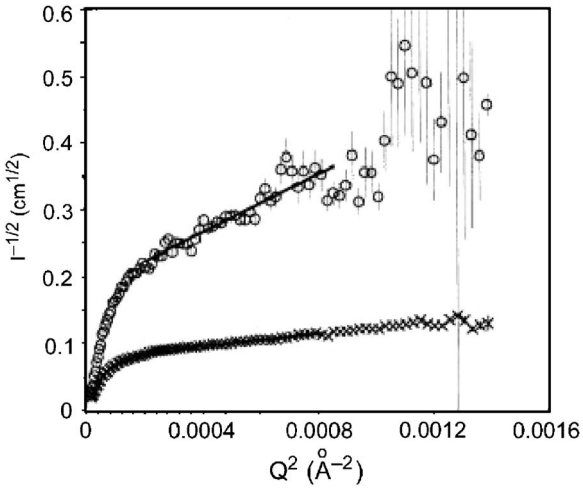

FIG. 12. Debye plot derived from a SANS experiment on a stack of Nanoglass™ thin films (with the silicon substrate attached). The open circles are for the as-received thin films, and the crosses are for the films immersed in *d*-toluene. The slope of the fitted line gives the correlatin length of the porous structure. The extrapolated intercept at $Q^2=0$ gives the poosity and the mass density of the pore wall material.

Homogeneous saturation of pores with a wetting liquid (e.g., *d*-toluene) should increase $\Delta\rho^*$ and result in a proportional increase of neutron scattering signal, leaving the shape of the function $[d\Sigma(Q)/d\Omega]$ unchanged. However, the SANS from the films immersed in *d*-toluene has a qualitatively different shape (see Fig. 12) and a smaller than expected increase in scattering, which suggests that the porous matrix is only partially filled with liquid. Calculations based on a two-layer model showed that the volume fraction of interconnected pores accessible to *d*-toluene is $22.1 \pm 0.05\%$. Application of the same two-layer model for SANS from films immersed in a non-wetting liquid (deuterated water) showed that water uptake is rather small ($3.10 \pm 0.05\%$ at room temperature.

Hedden *et al.*[95] applied the vapor adsorption SANS contrast variation technique to characterize properties of thin film low-*k* materials [methylsilsesquioxane (MSQ) and hydrogensilsesquioxane (HSQ)]. Utilizing the vapor adsorption is much more complicated than a simple immersion of a porous sample in a liquid as it requires a setup capable of delivering vapor mixtures with a variable composition of *h*/*d* solvent. Contrast variation was conducted by filling the pores with mixtures of deuterated and protonated toluene via vapor adsorption. Two streams containing saturated *d*- and *h*-toluene vapor were combined and passed through a SANS sample cell. The composition of the vapor was varied incrementally by controlling the relative flow rates of *d*- and *h*-toluene streams. For the MSQ film, the scattered intensity passed through a minimum at 0.22*d*-toluene/0.78*h*-toluene. At this point, a small coherent scattered intensity remained over the entire measured Q range. The contrast matching point of MSQ corresponded to SLD of $(2.0 \pm 0.11) \times 10^{10}$ cm^{-2}, which translates into the matrix mass density 1.97 ± 0.11 g/cm^3. In contrast, the scattering behavior of the HSQ dielectric film was found to be different in various Q

domains. The broad peak in the intermediate Q region $0.03-0.1$ Å^{-1} disappeared near a solvent fraction $0.5d$-toluene/$0.5h$-toluene: however, the strong upturn at low $Q<0.02$ Å^{-1} remained present at all solvent compositions. As was mentioned above, the upturn at small Q may be due to compositional inhomogeneities or closed pores. In the absence of a detailed knowledge of the physical reasons for the upturn, the density of the HSQ matrix may be estimated, considering the data only at $Q>0.4$ Å^{-1}, which gives a matrix SLD$=2.9\times10^{10}$ cm^{-2} and a corresponding matrix mass density of 2.12 g/cm^3. This value may be close to the actual average matrix mass density if the compositional inhomogeneities occupy only a small volume fraction of the sample.

Neutron porosimetry exploits the neutron contrast matching method and is based on the phenomenon of adsorption and condensation in small pores. A porous film is exposed to a solvent vapor having the same neutron SLD at the porous matrix. At any given partial pressure, pores are filled with the condensed liquid solvent, with the SLD matching that of the matrix. The coherent scattering therefore largely arises from the contrast between the empty and filled pores. Because the smallest pores are filled first (at low relative pressure), followed by progressively larger pores, the SANS characterizes subpopulations of pores of increasing average size. SANS experiments at increasing pressure (sorption) or decreasing (desorption) pressure can be performed at different temperatures. Hedden *et al.*[96] applied neutron porosimetry to extend studies of the structure of low-k MSQ thin films. A previously determined "contrast match" solvent mixture of $0.22d$-toluene/$0.78h$-toluene was chosen as a "probe" solvent. The relative pressure of the solvent was varied by mixing the air and solvent vapor streams at different flow rates at constant temperature (PV porosimetry) or by changing the temperature of the saturated film (TV porosimetry). The measured cross section was fitted to Eq. (18), and it was shown that the DAB model adequately describes the experimental data at all relative pressures and temperatures. A clear hysteresis in the sorption-desorption behavior of the correlation length ξ as a function of relative pressure was observed using the PV method. The behavior of the correlation length measured using TV porosimetry also exhibited a hysteresis. However, the absolute values of ξ were found to be significantly different from those obtained via the PV method, which indicated that the pore filling processes in PV and TV types of experiments must follow different pathways as a function of relative pressure.

Due to obvious limitations of the accuracy of standard characterization techniques (e.g., gravimetric and volumetric) when dealing with extremely small samples, the outlined methods of SANS measurements of the structure of thin films are becoming increasingly popular for a structure evaluation of a variety of thin films of practical importance such as low-k polyphenylene,[97] ordered mesoporous silica,[98] and proton exchange membranes.[99] A combination of SANS and mesoscopic computer simulation techniques seems to be the most promising approach for the morphology evaluation of the complex multiphase media.[100,101]

2. Fluid adsorption in porous media

A supercritical fluid (SCF) is a substance at a pressure and temperature above its liquid-gas critical point, where the coexisting (subcritical) liquid and gaseous phases become indistinguishable. At high pressures, the density of a SCF may become sufficient to provide substantial solvent power. At the same time, the diffusivity of solutes in SCFs is higher than in liquids due to a much lower viscosity, which facilitates mass transfer. The combination of tunable solvent power, practically unlimited miscibility with gases, as well as advantageous mass transfer properties make SCFs an attractive alternative to subcritical (liquid) solvents for a variety of technological applications such as supercritical extraction, heterogeneous catalysis, adsorptive separations, regeneration of adsorbers, and SCF chromatography. In most of the SCF-based technologies, fluid molecules interact with the surface of the porous materials, and these interactions may often lead to the creation of an "adsorbed phase" with properties different from those of the bulk (i.e., unadsorbed) fluid at similar thermodynamic conditions.[102] Regrettably, information on the physical properties of the adsorbed phase and their variation with pressure (P) and temperature (T) is inaccessible to conventional experimental methods (volumetric, gravimetric, etc.) which measure solely the *excess* adsorption n_e. It is related to the actual amount of the adsorbed fluid (*absolute* adsorption n_a) as

$$n_e = n_a(1-\rho_2/\rho_3) = n_a - V_3\rho_2. \tag{18}$$

Here, ρ_2 and ρ_3 are the densities of the unadsorbed and adsorbed fluid phase, respectively, and V_3 is the specific volume of the adsorbed phase in cm^3/g. Equation (18) shows that the absolute adsorption can be rigorously calculated from n_e only if the density or the volume of the adsorbed phase is known. Because this information is not readily available, different assumptions are usually made to calculate n_a, such as $\rho_3 \gg \rho_2$ at all pressures and temperatures, in which case $n_a \approx n_e$.

Scattering experiments have an advantage of probing the properties of imbibed fluids on a nanoscale level. As was mentioned in the previous paragraph, SANS has been widely used to characterize the structure of porous materials by saturating them with contrast matching liquids or applying contrast variation methods. It has also been applied to investigate the influence of confinement on the phase behavior of binary liquid solutions and individual fluids.[103–108] Melnichenko *et al.*[109] applied SANS along with the neutron transmission techniques to characterize the adsorption of SC CO_2 in aerogels with a nominal density of $\rho_{\text{aerogel}}=0.1$ g/cm^3, corresponding to ~96% porosity. The neutron transmission is a parameter routinely measured in SANS experiments. It is one of the factors used for converting the intensity of scattering in counts/s into a neutron cross section in units of cm^{-1}. By definition, neutron transmission (T) is the ratio of the transmitted beam intensity after attenuation by the sample to the incident neutron intensity. The transmission of a three-phase system which consists of the porous aerogel (phase 1), unadsorbed fluid (phase 2), and adsorbed fluid phase (phase 3) is given by

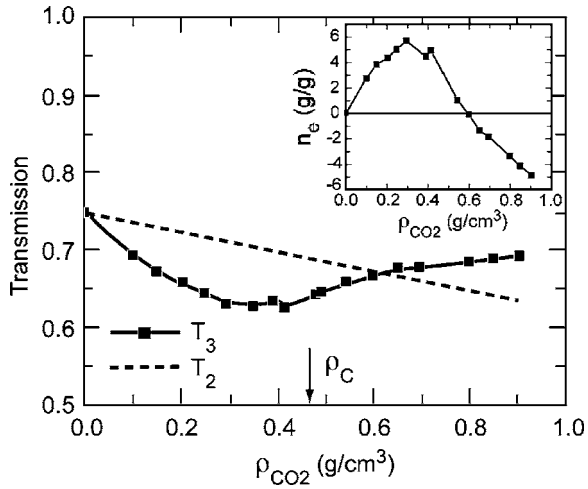

FIG. 13. Transmission of the CO_2-saturated aerogel without and with the adsorbed phase (T_2 and T_3, respectively) as a function of the fluid density. The inset shows the variation of excess adsorption n_e as a function of ρ_{CO_2}.

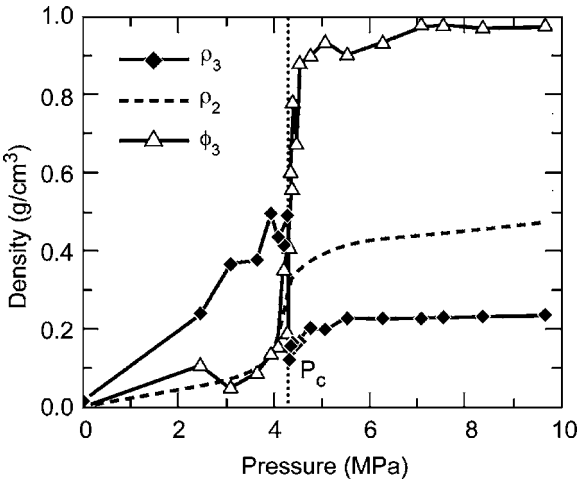

FIG. 14. Density of the unadsorbed and adsorbed *d*-propane in aerogel (ρ_2 and ρ_3, respectively) as a function of pressure. Hollow triangles represent the pressure dependence of the volume of the adsorbed phase.

$$T_3 = T_2(\exp - N_e \sigma_{CO_2} l), \tag{19}$$

where T_2 is the transmission of the two-phase system representing an aerogel homogeneously saturated with CO_2 (no adsorption), N_e is the number density of CO_2 corresponding to the excess adsorption, $\sigma_{CO_2} = 14.01 \times 10^{-24}$ cm^2 is the total neutron cross section of a CO_2 molecule, and l is the sample thickness. SANS and transmission measurements of aerogels saturated with SC CO_2 were performed along several isotherms as a function of pressure in the range $0 \leqslant P \leqslant 25$ MPa, which corresponded to the bulk fluid densities in the range $0 \leqslant \rho_{CO_2} \leqslant 0.9$ g/cm^3. Figure 13 shows the variation of transmissions T_2 and T_3 as a function of the fluid density at $T = 35$ °C, i.e., about 4° degrees above the critical temperature of the bulk fluid. A strong *negative* deviation of T_3 from T_2 was observed due to the formation of the adsorbed phase, with the density $\rho_3 \sim 1.07$ g/cm^3 much higher than the density of the unadsorbed fluid at similar thermodynamic conditions ($\rho_2 = 0.3$–0.4 g/cm^3). The parameters T_2 and T_3 were used to calculate N_e via Eq. (19) and thus the excess adsorption parameter n_e using:[109]

$$n_e = \frac{M_{CO_2} N_e}{\rho_{\text{aerogel}} A_0}, \tag{20}$$

where $M_{CO_2} = 44.01$ is the molecular weight of a CO_2 molecule and A_0 is Avogadro's number. The values of n_e thus determined are shown in the inset in Fig. 13. The data demonstrate that the maximal excess adsorption capacity of aerogel ($n_e \sim 5.74$ g/g) far exceeds n_e for CO_2 in other adsorbers such as zeolites and activated carbon ($n_e \sim 0.2$ and 0.9 g/g, respectively) due to much higher porosity and an "optimal" mesh size ~60 Å of the studied aerogel.

The volume fraction of the adsorbed phase ϕ_3 can be calculated using the theory of scattering from three-phase systems initially developed by Wu[110] to model scattering from microvoids in composite materials,

$$\phi_3 = \frac{Z_3 - Z_2}{2\pi^2[\phi_2(\rho_2^* - \rho_3^*)^2 + \phi_1(\rho_1^* - \rho_3^*)^2 - \phi_1(\rho_1^* - \rho_2^*)^2]} = \frac{\rho_p - \rho_2 \phi_2}{\rho_3}, \tag{21}$$

where Z_2 and Z_3 are invariants for a two-phase and a three-phase system, respectively, ϕ_i are the volume fractions, and ρ_i are scattering length densities of the ith phase. Neutron transmission measurements can be used to determine the "mean" fluid density in adsorbent pores ρ_p and to eliminate the unknown volume fraction of the unadsorbed phase ϕ_2 in Eq. (21). Thus, both the density ρ_3 and volume fraction ϕ_3 of the adsorbed phase can be determined from SANS and transmission measurements at different pressures and temperatures.

This approach was applied by Rother *et al.*[111] to quantify the adsorption of supercritical propane in the silica aerogel and determine the variation of ϕ_3 and ρ_3 as a function of pressure. The aerogel was the same as that used in the previous study of the adsorption of SC CO_2 Ref. 109, and deuterium substituted propane with deuteration degree of 99.5% was used to minimize significant incoherent background from hydrogen in normal (protonated) propane, which would inhibit measurements of the coherent SANS signal from the fluid saturated aerogel. The variation of ρ_3 and ϕ_3 of *d*-propane in the aerogel at near-critical temperatures of the fluid $T_C = 91 \pm 0.1$ °C is shown in Fig. 14, which demonstrates that in the low pressure region P below the critical pressure of *d*-propane $P_C \cong 4.25$ MPa, the density of the adsorbed fluid phase increases almost linearly with pressure. At the same time, the volume fraction of the adsorbed phase remains approximately constant $0.06 \leqslant \phi_3 \leqslant 0.1$ and independent of P. The density of the adsorbed fluid is nonmonotonic: just below P_C, it reaches a maximum of $\rho_3 \approx 0.5$ g/cm^3, which is close to the density of liquid propane. At $P > P_C$, ρ_3 decreases down to 0.23 g/cm^3, becomes lower than the density of unadsorbed phase, and remains independent of P up to 10 MPa. Conversely, the volume fraction of the adsorbed phase increases monotonically with pressure for

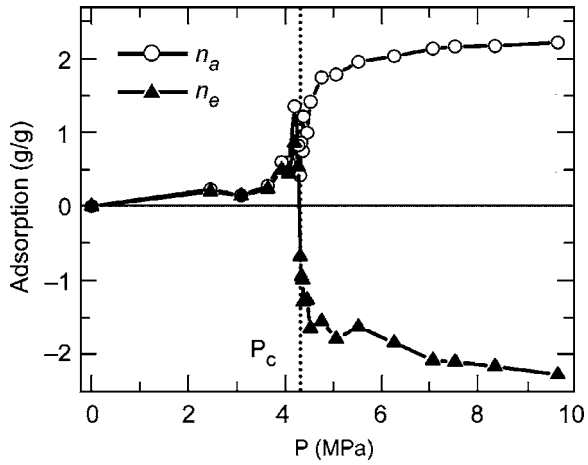

FIG. 15. Excess and absolute adsorption parameters of *d*-propane in aerogel as a function of pressure.

$P < P_C$ and approaches $\phi_3 \sim 0.96$ at $P \gg P_C$, which indicates that at high pressures the entire pore volume is filled with the adsorbed fluid with $\rho_3 < \rho_2$.

The excess adsorption n_e was calculated from the transmission data using Eqs. (19) and (20), and the absolute adsorption n_a was calculated via Eq. (18). The variation of n_e and n_a, as a function of pressure, is shown in Fig. 15. At $P < P_C$ all parameters are increasing functions of pressure with maximum values reached at $P \sim P_C$ due to critical adsorption.[112] At or above P_C the excess adsorption decreases rapidly and becomes negative, which correlates with the observed ratio $\rho_3/\rho_2 < 1$ in this region (see Fig. 14). The variation of n_e for SC CO_2 and SC *d*-propane with pressure is qualitatively similar and reveals the depletion of aerogel pores (i.e., negative values of the excess adsorption) at pressures above P_C of the bulk fluid. The data provide unequivocal experimental evidence for a tendency of supercritical fluids to be expelled by a confining medium, which manifests itself as a significant decrease of the excess adsorption. Additionally, the results demonstrate that the depletion of the aerogel is not restricted to the critical region and may extend over a wide range of pressures and densities above P_C and ρ_C. Unfortunately, computer simulation and theoretical studies of the fluid depletion in pores are extremely limited[113,114] and have not yet provided a convincing explanation of this remarkable behavior. From a practical point of view, experimental results[109,111] demonstrate that the assumption $\rho_3 \gg \rho_2$, which as discussed above is often used to calculate n_a from n_e, may not always be valid as ρ_3 may be a nonmonotonic function of pressure and may become lower than the density of an unadsorbed fluid at high pressures.

The described examples illustrate the fact that SANS, in conjunction with transmission measurements, may be used as a very effective characterization method that allows us to extract unique information on the adsorption behavior of various single-component fluids in different adsorbents of practical importance. The methodology developed in Refs. 109 and 111 can also be extended to adsorption studies of supercritical fluid *mixtures* in porous materials using deuterium-labeling methods of one of the components. One of the interesting applications of the described methodology might be in the investigation of the interactions between carbon dioxide as well as methane molecules and various coals at different temperatures and pressures. The results of such studies could be important in developing technologies of sequestration of CO_2 in deep coal seams as well as in the methane drainage industry.[115]

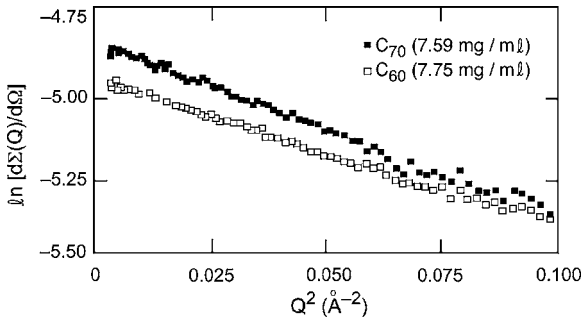

FIG. 16. Guinier plots for C_{60} and C_{70} fullerenes in CS_2 at the fullerene concentration shown in the inset.

3. Dispersions of fullerenes and carbon nanotubes in solution

The discovery of C_{60} (Ref. 116) and carbon nanotubes[117] has generated significant interest in the basic and applied research communities due to the well defined and highly stable structure of carbon nanostructures as well as their possible applications in tribology, photoconductivity, nuclear medicine, superconductivity, plastic reinforcement, etc. Of particular interest is the information on interactions of C_{60} and other fullerenes with different solvents as well as their possible polymerization into interconnected or dangling chains, which can drastically modify the solution properties. Because the characteristic sizes of fullerenes are within the SANS resolution range, this technique is capable of providing information on the shape of the fullerene species (spherical, ellipsoidal, tubular, etc.) as well as solvent-solute and solute-solute interactions in solutions. SANS studies of fullerenes were initiated by Affholter *et al.*,[118] who investigated the structure of C_{60} and C_{70} in CS_2. The choice of a solvent for such studies is not trivial because C_{60} is known to have limited solubility in organic solvents (e.g., 1.7 mg/ml in benzene, 2.8 mg/ml in toluene, 7.9 mg/ml in CS_2, etc.). Protonated solvents cannot be used as they give rise to high background scattering due to the large incoherent cross section of hydrogen. Finally, because of the limited fullerene solubility, the signal-to-noise ratio should be maximized by using a solvent with a substantial scattering contrast with the particles. Because the deuterated counterparts of most of the available solvents have virtually no scattering contrast with carbon (see Table I), CS_2 comes closest to satisfying the above criteria. The Guinier approximation for independently scattering particles is[13]

$$\frac{d\Sigma(Q)}{d\Omega} = \frac{d\Sigma(0)}{d\Omega} \exp\left(-\frac{Q^2 R_g^2}{3}\right), \tag{22}$$

where R_g is the radius of gyration (i.e., the root-mean-square distance of all scattering elements from the center of gravity). Figure 16 shows Guinier plots $\ln(d\Sigma/d\Omega)$ vs Q^2 for C_{60}

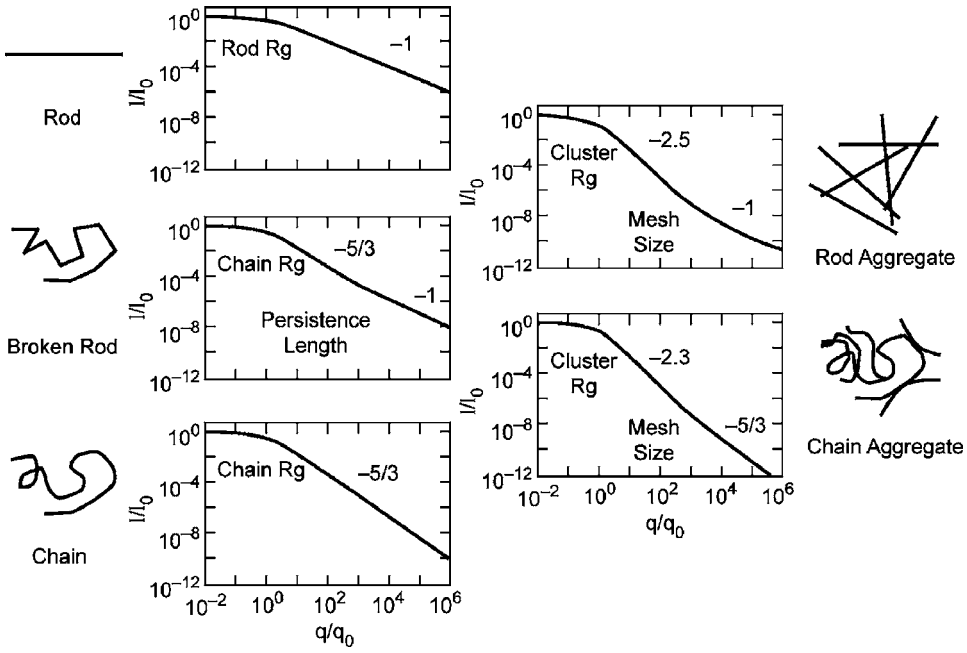

FIG. 17. Power law scattering from several fractal objects.

and C_{70} in CS_2. The slope in this figure is proportional to R_g and is higher for the C_{70} particles than the C_{60} fullerenes. Fitting the data to Eq. (21) gave the values of $R_g = 3.82 \pm 0.05$ Å for C_{60} and $R_g = 4.13 \pm 0.05$ Å for C_{70}, the former being later independently confirmed in SANS experiments by Migliardo *et al.*[119]

SANS studies of the structure and interactions of fullerene solutions were continued by Melnichenko *et al.*,[120] who extended experiments to higher fullerenes (C_{84}) and determined the second virial coefficient of C_{60} solutions in CS_2. The same experimental strategy as in a previous study[119] was applied to determine R_g of C_{84}. However, this time, the SANS data were fitted using both the Guinier formula [Eq. (22)] and a spherical shell model (SSM).[121] The analysis has shown that due to a limited Q range covered in SANS experiments, Guinier fits lead to ~8% overestimated values of R_g for C_{84}, whereas fits to the SSM model over, extended Q range gave $R_g = 4.27 \pm 0.06$ Å, which agrees well with the results of the molecular modeling calculations. The second virial coefficient of CO_{60} solutions in CS_2 at room temperature determined from the SANS using Eq. (8) was found to be zero within the experimental error, which shows that to a good approximation both particle-particle and particle-solvent interactions can be neglected in the studied system. The results of these experiments demonstrate that SANS can accurately resolve individual fullerenes in solutions with as few as 60 atoms, although the measured dimensions are close to the resolution limit of the technique. The larger particles (higher fullerenes, flagellenes, molecular-colloidal solutions of fullerenes,[122] carbon nanotubes, etc.) are progressively easier to study as the coherent neutron cross section is a strong function of the particle dimensions $R(d\Sigma/d\Omega \sim R^6)$,[13] so that bigger particles will have much higher scattering cross sections compared to incoherent and instrumental background signals.

Isolated single-walled carbon nanotubes (SWNTs) are one-dimensional objects with diameters of 1–2 nm and lengths ranging from ~100 nm to several microns. Many of the potential applications of SWNTs involve their dispersion in liquids or solid matrices. Current synthetic methods produce SWNTs in bundles, which need to be separated to produce individual nanotubes that can be sorted and manipulated. One route to disperse SWNTs involves chemical functionalization of their walls by reactive groups, which enhance compatibility with the surrounding medium. Alternatively, physical approaches using amphiphilic surfactants (dispersants) have been proven capable of separating SWNT bundles and stabilizing individual tubes without perturbation of the intrinsic nanotube's structure caused by chemical modification. In both cases understanding the resulting morphology of nanotubes in dispersions should lead to a better control of the solution structure and optimization of the physical properties of SWNT composites.[123]

Small-angle scattering techniques are ideal for investigating the structure of SWNTs in solutions. Figure 17 shows a collection of model fractal structures and the resultant small-angle scattering from individual one-dimensional rigid and flexible objects as well as from their aggregates.[124] As was pointed out in Sec. III A 1, the scattering cross section from a dispersion of isolated rigid rods should follow a Q^{-1} law in the limit of high Q [see Eq. (10)]. If a number of rods are brought together to form an aggregate, the resultant branched structure is characterized by the exponent α with the values between 2 and 3 in the intermediate Q range.[125,126] Zhou *et al.*[127] used SANS to characterize the structure of SWNT dispersions in D_2O with an added sodium dodecylbenzene sulfonate surfactant. They demonstrated that in dilute well dispersed suspensions the scattering varies as the Q^{-1} characteristic of isolated rigid rods. In more aggregated dispersions a power law with exponents between 2 and 3 was observed over the entire range of measured Q, suggesting the formation of branched aggregates. Wang *et al.*[128] studied dispersions of SWNTs in D_2O with the surfactant octyl-phenol-ethoxylate (Triton X-100) and demonstrated that the expo-

nent α varies in the range $2.8 > \alpha > 1.8$, a function of the surfactant concentration with a minimum corresponding to 0.5% to 1% of Triton X-100. The availability of $\alpha_{\min} \sim 1.8$ was treated as an optimal condition for the dispersion arising due to a balance between surfactant adsorption onto SWNT surfaces and a micelle-mediated reduction of interactions between adjacent SWNT bundles. Bauer *et al.*[124] used a high-concentration labeling method to extract single-particle scattering from SWNT dispersions. While, in principle, SWNTs could be made of ^{12}C and ^{13}C, the neutron contrast between these isotopes is quite small compared to the difference between hydrogen and deuterium. Because SWNTs themselves contain no hydrogen, deuterium substitution cannot be used on them alone, as in the case of polymers (see Sec. II A). Thus, SWNTs were labeled by covalently attaching alkyl C_4H_9 or C_4D_9 groups using free radical chemistry. Mixtures of SWNT-C_4H_9 and SWNT-C_4D_9 were dispersed in D_2O containing 1% sodium lauryl sulfate-d_{23} by the use of sonification. The SLD of the surfactant matches that of D_2O, and thus all measured SANS comes from the labeled SWNT, which was found to follow the $Q^{-2.5}$ power law. Based on these results a conclusion was made that the "single-particle" scattering measured in the study was not from individual nanotubes but rather from clusters of nanotubes which remained unseparated in solution despite vigorous sonication. It was assumed that the persistent aggregation may be due to a high-energy free radical chemistry involved in the labeling reaction.

Despite numerous efforts, the problem of effective debundling of carbon nanotubes and obtaining homogeneous single-tube dispersions is far from being resolved. It has been suggested[129] that dispersion of the large quantities of isolated nanotubes may be achieved by using block copolymers with selective interactions of the different blocks with the solvent. In this case hydrophobic blocks get adsorbed on the SWNT surface, whereas the hydrophilic blocks may serve as steric barriers preventing the tube interactions. Early SANS experiments seem to support this assumption.[130] SWNT/dispersant combinations specifically tailored for the fabrication of future high-performance SWNT nanocomposites will require a detailed understanding of their structure. The ability of SANS to provide information on the local structure and interactions allows us to expect that this technique will remain as one of the premier methods for the characterization of these complex structurally hierarchical systems.

IV. USANS AND NEUTRON RADIOGRAPHY

A. Material morphologies on the micrometer length scales

As mentioned before, a typical range of scattering vectors covered by conventional SANS instruments is $10^{-3} < Q < 1$ Å^{-1}, which corresponds to the structural length scales of 10–1000 Å. This resolution is more than sufficient for studying structure of many systems such as polymer solutions where the upper limit of the radius of gyration is typically $R_g \sim 500$–600 Å, which satisfies the limit of the Guinier approximation ($QR_g \leq 1$). However, in many materials such as polymer composites, protein hydrogels, mesoporous materials, bones, cements, colloids, rocks, and clays, structural inhomogeneities may span length scales from nanometers to microns, and a complete characterization of such hierarchical structures at all levels requires the application of complementary neutron scattering methods with an adequate resolution. The wide-angle neutron scattering (WANS) diffractometers cover the Q range corresponding to atomic scattering. At the same time, ultrasmall-angle neutron scattering (USANS) instruments can extend characterization capabilities to access length scales up to several microns.

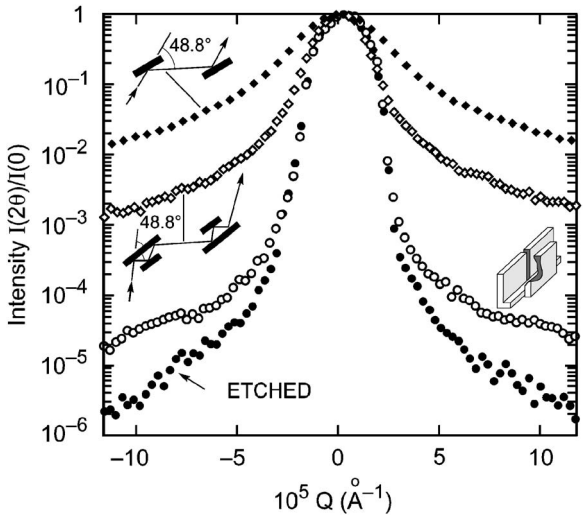

FIG. 18. Rocking curves for single- and triple-bounce crystals. Addition of a Cd adsorber prevents neutron propagation inside the Si walls and greatly improves the USANS sensitivity. Etching removes surface imperfections and further enhances the signal-to-noise ratio.

The required Q resolution for USANS can be achieved using double-crystal diffractometers (DCDs) with channel-cut perfect crystals. This so-called Bonse-Hart technique[131] has been employed since 1965 for ultrasmall-angle x-ray scattering. The reflectivity function of a single crystal and, thus, the rocking curve of the DCD have an extremely narrow angular resolution of the order of a few arcseconds, which provides an opportunity for measuring the USANS from a sample placed in between the monochromator and analyzer crystals of the DCD. However, the single-bounce reflectivity curve has rather intense tails (or wings), which significantly decrease the signal-to-noise ratio of the DCD and thus diminish the sensitivity of scattering from a sample in the Q range of the wings (see Fig. 18). The first attempts to apply the Bonse-Hart technique with neutrons[132,133] had only a limited success because of the incomplete suppression of the wings of the rocking curve as well as relatively low neutron fluxes generated by nuclear reactors compared with available x-ray sources. The low flux is partly compensated by the larger sizes of neutron beam. However, about two orders of magnitude lower signal-to-noise ratio remained as a main USANS limitation. The major progress in developing an effectively operating USANS diffractometer was made after Agamalian *et al.*[134] discovered that the reason for the low sensitivity of DCD was a contamination of the rocking curve wings by the single-bounce back-face reflection in the triple-bounce crystals. Thus, channel-cut crystals were modi-

fied to include neutron absorbing components (Cd) to block this parasitic reflection which made USANS rocking curve parameters comparable to those of USAXS. In addition, etching the crystals to remove surface imperfections further enhances[135] the sensitivity by another order of magnitude (Fig. 18). These improvements in the signal-to-noise ratio allowed for an extension of the studies of structural inhomogeneities with dimensions up to 10–30 μm, thus overlapping with light scattering techniques.

At present, the reactor-based Bonse-Hart USANS instruments are installed at virtually all major neutron scattering facilities such as the National Institute of Standards and Technology (NIST, USA, Japanese Atomic Energy Agency), Hahn-Meitner Institute in Berlin, Institute Laue-Langevin, France, and Atominstitut, Austria. The world's best BT-5 USANS at NIST (Ref. 136) equipped with a double-focusing PG premonochromator delivers a neutron flux of $\sim 17\,000\ n/(\mathrm{cm}^2\ \mathrm{s})$ at the sample position and reaches a sensitivity of $I(Q=5\times10^4\ \text{Å}^{-1})/I(Q=0)\sim5\times10^{-7}$. It covers the dynamical Q range of $3\times10^{-5}<Q<2\times10^{-2}\ \text{Å}^{-1}$ overlapping with that of the conventional pinhole SANS, which permits conducting a combined SANS/USANS experiments even for weakly scattering samples.

It is now recognized that about a half of the materials problems in a wide range of scientific disciplines require obtaining structural information on the length scales covered by both SANS and USANS (Ref. 137), and these techniques have been widely used in tandem in investigating structure-property relationships in polymer blends, colloids, coals, complex fluids, hydrogels, porous materials, nanocomposites, and cements. The results of combined SANS/USANS studies in the field of materials science were reviewed in recent papers by Schaefer and Agamalian[138] and Agamalian[139] and we refer an interested reader to these articles. Here, we will give only one illustrative example of the combined USANS/SANS/WANS study of the local and large scale (global) structure of a strongly aggregating polymer system representing a gel-forming solution of polyvinyl alcohol (PVA) in deuterated water D_2O.[140,141] Here, the multiscale structural organization is induced by deterioration of the solvent quality, which results in the formation of a complex hierarchical morphology. The neutron scattering $I(Q)$ measured from a PVA gel over a wide Q range from 10^{-4} to $10^{-1}\ \text{Å}^{-1}$ using several neutron scattering methods is shown in Fig. 19. WANS measurements at $Q<1\ \text{Å}^{-1}$ revealed Bragg peaks, which means that the cross-links of the gel represent microcrystallites. In the "intermediate" range of scattering vectors ($0.01–0.1\ \text{Å}^{-1}$) accessible to SANS, the neutron cross section can be described by the Ornstein-Zernike equation (15), and thus the size of the microcrystallites ($\sim$70 Å) can be determined. USANS data in the Q range below $0.008\ \text{Å}^{-1}$ reveal a strong upturn, suggesting the existence of even larger structures induced by liquid-liquid phase separation. These structures formed during the final stage of the phase separation, according to the USANS data, have a characteristic length scale $\sim1.8\ \mu$m. Figure 19 illustrates the importance of applying neutron scattering methods with various resolutions for a full multiscale characterization of complex systems.

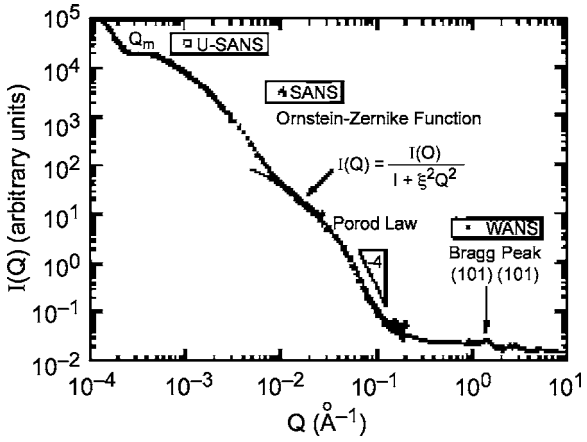

FIG. 19. Combined USANS, SANS, and WANS data for a PVA gel saturated with D_2O.

B. Neutron imaging of macroscopic structures and operational devices

As demonstrated in the previous paragraph, the diffractive neutron scattering methods (WANS, SANS, and USANS) can deliver information on the molecular arrangements and correlations in the range of length scales between fractions of nanometer up to tens of microns. This range can be further extended up to a macroscopic scale (millimeters and centimeters) by the use of neutron transmission radiography (NTR), which represents a nondiffractive method of direct imaging currently employed in a variety of industrial applications. Due to a high penetration power, neutrons can be used for nondestructive imaging as they are able to penetrate thick material layers. High interaction probability (scattering and adsorption) of thermal and cold neutrons with light elements, in general, and hydrogen, in particular, allows us to resolve the distribution of small amounts of organic substances and to determie hydrogen concentration inside various inorganic materials including many metals [the measurable lower limit of hydrogen concentration is as low as $\sim$100 ppm (Ref. 142)]. The ability to detect light elements inside heavier ones has been used for many years for routine quality assurance testing, inspection, and internal characterization of pyrotechnic devices, investment-cast turbine blades, and radioactive assemblies.[143]

Generally, a NTR setup consists of a suitable neutron source, a collimator delivering neutrons to the sample, and a two-dimensional area detector registering the transmitted beam behind the sample. Thus, images or radiographs recorded by the detector represent shadow images of the neutron beam resulting from attenuation of the neutrons passed through the sample. The traditional application of NTR can only provide information on the total attenuation integrated over the path of the radiation through the material. The actual distribution of materials across that path can be determined using neutron tomography which provides three-dimensional (3D) images of the material distribution in various objects via computer reconstruction of a number of two-dimensional (2D) NTR images of the sample taken from different perspectives.[144] An example of 3D neutron tomography is given in Fig. 20, which shows a small pyritized

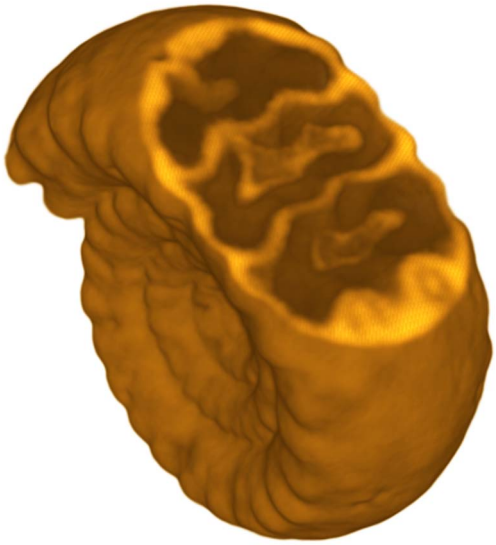

FIG. 20. (Color online) A cross section of a small ammonite through a 3D volume provided by neutron tomography.

FIG. 21. Snapshot of a running BMW car engine operating at 1000 rpm.

ammonite with an outer diameter of 21 mm and a thickness of 10 mm. In order to get a 3D neutron tomography image of ammonite, 240 projections with a 0.75° angle increment were recorded, and individual slices were combined using a filtered back-projection algorithm.[145] In addition to obtaining static 3D images, the NTR can be used for recording periodic processes. Today's neutron sources do not deliver fluxes sufficient for getting snapshots of relatively fast processes in the millisecond range. However, repetitive motions can be recorded using a stroboscopic approach where taking the image is synchronized with a specific position of a moving object undertaking a cyclic motion, until sufficient statistics are accumulated. The first experiments of this type were carried out at the Institut Laue-Langevin, France with the purpose of visualizing the functioning of a four-piston BMW car engine electrically driven by a 2 kW electric motor.[146] The full cycle of the four-stroke engine running at 1000 rpm was split into 120 individual time frames, and 150 individual NTR images were recorded with 200 μs exposure for each frame. Figure 21 shows a single snapshot of this recorded movie which allowed us for the first time to watch the engine work "from the inside" in real time.[147]

In addition to the above mentioned industrial applications, neutron testing and imaging techniques are routinely used in examining geological and construction materials,[145,148,149] archeology,[150] metallurgy,[151] as well as water flow and diffusion in soil[142] and engineered porous materials.[152] One of the most recent applications of NTR is *in situ* measurements of the water transport in operating proton exchange membrane fuel cells. Such studies help to visualize the areas of water accumulation and to determine the water concentration profiles through the membrane at different operating conditions, which makes it possible to identify primary water transport mechanisms in the gas diffusion medium. Hence, the NTR can provide important information necessary to validate models of fuel cells, to find the materials and operating conditions for optimal water management, and to provide insights required for developing fuel cells for the next generation.[153–160]

V. OUTLOOK

This section summarizes the findings of a panel discussion,[161] which was held to discuss cutting edge research, in addition to predictions and prospects for future developments in the field. However, the first requirement of current and future research is to have access to SANS facilities, many of which are currently located at 20–40 year old reactors, and may become unavailable in the next one to two decades. The first modern SANS instrument[162] was built in the late 1960s at the FRJ2 reactor at the Forschungszentrum, Jülich, Germany and pioneered the use of long wavelength neutrons and large overall instrument lengths (~40 m) in order to maintain resolutions in the range 10–2000 Å. It was also the first to boost the flux of the long wavelength ($\lambda > 4$ Å) component of the Maxwellian spectrum by moderating the neutrons to a lower temperature by means of a cold source containing liquid hydrogen at $T \sim 20$ K. This gives flux gains of over an order of magnitude at $\lambda \sim 10$ Å, and the D11 facility, built during the 1970s on the High Flux Reactor (HFR) at the Institut Laue-Langevin (ILL), Grenoble, France, incorporated many of the features of the FRJ2 instrument, including a cold source and long (~80 m) dimensions.[163] Both the FRJ2 and HFR instrumentations made use of neutron guide tubes, as proposed by Maier-Leibnitz and Springer,[164] and over the past three decades, these facilities have been among the most productive SANS facilities worldwide.

Subsequently, over 20 other SANS facilities have been constructed worldwide, though several of these instruments are no longer operational.[161] This trend can be expected to continue as many currently available facilities were constructed on reactors that were built in the 1960s and 1970s, and a forward survey in the late 1990s (Ref. 165) estimated that over the next two decades, the installed capacity of neutron beams for research could decrease to a level *below one*

third of the present capacity. Fortunately, the decline in the availability of reactor-based SANS instruments, as exemplified by the shutdowns of the Jülich, Brookhaven and Risø National Laboratory reactors, has been offset by two competing trends. Firstly, several new reactors have been recently built or are under construction worldwide (e.g., FRM Munich, Germany, Open Pool Australian Light-water Reactor, Lucas Heights, Australia), along with upgrades to existing sources (e.g., at the ILL in the mid-1990s, ORNL, and the Japan Atomic Energy Agency, Tokai during 2000–2007). In addition, a range of accelerator-based SANS instruments have been developed over the past 15 years, and in particular, a Spallation Neutron Source (SNS) has been constructed at Oak Ridge,[166] where it is currently being commissioned. In Europe, a second target station at ISIS (Ref. 167) will do much to offset and even reverse the predicted decline in the availability of SANS facilities. Thus, it seems likely that pulsed sources will make a much greater contribution to SANS investigations in the future than they have done in the past. Also, reactors have been optimized over the past several decades, and the flux of instruments planned on new or upgraded reactor sources will either be less than or equal to the current state-of-the-art instruments (e.g., at D22 at the ILL). However, this is not the case for pulsed facilities, which have not yet begun to reach their full potential, so we can still expect order of magnitude gains over the current facilities via the SNS, ISIS-2, etc.

New high flux sources will also provide the scientific community with an opportunity to design novel classes of nonequilibrium time-resolved studies and shear-induced phenomena. Processing is a key issue in enabling new materials and technology to reach the market place, and is also an area that lags behind synthesis and morphology. Deformation leads to changes in morphology that must be studied under actual conditions, and flow instabilities in polymer extrusion are often the most vexing problem in the commercialization of new products. The need for analyzing systems close to actual processing conditions has been recognized previously,[168] and neutrons have a unique advantage since they can penetrate macroscopic extruders and flow devices. Thus, SANS is the technique of choice for exploring the effects of flow in industrially relevant equipments.

USANS is also becoming increasingly popular in materials science research, though the main drawback of the existing Bonse-Hart instruments is that they do not measure two-dimensional scattering patterns (like SANS), and the data are taken in a slit geometry and are thus slit smeared. Alefeld *et al.*[169,170] proposed an alternative design using focusing toroidal mirrors (FTMs), and a demonstration instrument will shortly be commissioned at the new FRM reactor in Munich. The advantages of this design are that the FTM-USANS instrument is quite compact, and so count rates remain high, and that it measures 2D scattering patterns.

Further USANS instrumental gains can, in principle, be made by constructing a USANS difractometer on a pulsed source, as opposed to the facilities built on steady-state (reactor) sources described above. In particular, calculations[137] describing an instrument with triple-bounce Si channel-cut crystals show that significant gains in Q resolution and neutron flux can be achieved using multiple high order Bragg reflections. Thus, in a time-of-flight (TOF) USANS facility, neutrons will be Bragg reflected from a perfect crystal oriented at a fixed angle with respect to the "white" primary beam, with a series of wavelengths satisfying Bragg's law, $n\lambda_n = 2\ \mathrm{D} \sin\theta$ [see Eq. (1)], where $n = 1, 2, 3, \ldots$. Because the neutron speed V is inversely proportional to its wavelength, the time of arrival L/V is proportional to the wavelength, where L is the distance from the neutron source to the detector. The corresponding diffracted neutrons arrive at the detector at different times, well resolved because of the short source pulses. This provides a simultaneous parallel measurement of the USANS signal: using, say, up to eight different wavelengths could lead to significant intensity enhancement compared to using the monochromatic reactor-based USANS instruments. Moreover, a second significant aspect of the TOF-USANS technique is that because the angular resolution (the rocking curve width) is proportional to λ^2, the use of high-order diffraction peaks allows the achievement of significantly higher Q resolution than the use of only one low-order reflection.[137] Thus, using multiple wavelengths could dramatically extend the value of $Q_{\min}$ from $\sim 2\times 10^{-5}$ to $\sim 4\times 10^{-6}$ Å^{-1}, which will allow measurements of enormously large inhomogeneities with dimensions up to 200 μm.[137] Based on these principles, a TOF-USANS facility is planned at the new SNS source and may be expected to improve the current state of the art and open up a whole new area of science at the neutron/light scattering interface.

In order to assess the utility of forecasts of future developments in the field, as attempted in this article, it may be instructive to review previous attempts to do so. Then, as now, the availability of SANS facilities was a concern and it was hoped that there would be an approximate doubling of the number of reactor neutrons incident on samples "over the next decade."[171] This prediction has come closer to realization in Europe, where the commissioning of new instruments at the ILL (Grenoble), Hahn-Meitner Institute (Berlin), FRM (Munich, Germany), and Paul Scherrer Institutes (Switzerland) has more than offset the loss of the Risø and Jülich reactors. However, in the US, the cancellation of the advanced neutron source and the shutdown of the Brookhaven source has largely negated the forecast that polymer scientists will be more prone to use the technique with increased beam time availability.[171] NIST has remained as the main "workhorse" for SANS research and projections that "increased flux will lead to a proliferation of kinetic and time-resolved studies" will have to await new and upgraded facilities before they are fully realized.

On the other hand, predictions[172] that absolute calibration will become routine, that the gap between SANS and light scattering will be closed, that the equipment will be more user-friendly as changes in the sample-detector distance and beam collimation will be more easily accomplished, and that faster computers will permit a real-time analysis and comparison with theory have been largely authenticated. In addition, the forecast that solid state detectors will be developed for a better Q resolution and/or a more compact equipment has been partially fulfilled, as new high-

count-rate area detectors have been constructed for the FRJ2, ILL, and Oak Ridge SANS instruments. Further developments along these lines could be of even greater importance for the future of pulsed SANS facilities.

Lastly, advances in other areas of scientific equipment design have generally resulted in more compact apparatus while retaining, or even improving, on resolution, etc. In the future there seems to be no reason why an experimentalist should not simultaneously measure the UV/vis or IR signature of a sample, or even its small-angle x-ray scattering, at the same time as the SANS data are recorded. Exploiting the complementarity of different techniques in this way will prove significant in areas such as biopolymers and polymer crystallization, to name but two.

ACKNOWLEDGMENTS

The authors would like to thank P. Vontobel and B. Schillinger who provided Fig. 20 and 21, respectively, and gave their comments on the chapter describing the applications of neutron transmission radiography. The authors have benefited from long-standing collaborations with M. M. Agamalian and D. W. Schaefer with whom they had discussions and correspondence on USANS applications in materials science. This research is sponsored by the Division of Materials Science, U.S. Department of Energy under Contract No. DE-AC05-00OR22725 with the Oak Ridge National Laboratory, managed by UT-Battelle, LLC.

[1]G. D. Wignall and Y. B. Melnichenko, Rep. Prog. Phys. **68**, 1761 (2005).
[2]D. J. Lohse, Polym. News **12**, 8 (1986).
[3]S. K. Sinha, D. J. Lohse, and M. Y. Lin, Physica B **213-214**, 1 (1995).
[4]R. P. Kambour, R. C. Bopp, A. Maconnachie, and W. J. MacKnight, Polymer **21**, 133 (1980).
[5]H. Ito, T. P. Russell, and G. D. Wignall, Macromolecules **20**, 2213 (1987).
[6]P. Thiyagarajan, J. Appl. Crystallogr. **36**, 373 (2003).
[7]J. B. Hayter, Physica B **136** 269 (1986).
[8]J. B. Hayter and J. Penfold, Colloid Polym. Sci. **261**, 1022 (1983).
[9]J. B. Hayter, in *Physics of Amphiphiles, Micelles, Vesicles and Microemulsions*, edited by V. de Giorgio and M. Corti (North-Holland, Amsterdam, 1985).
[10]L. J. Magid, Colloids Surf. **19**, 129 (1986).
[11]S. H. Chen, Annu. Rev. Phys. Chem. **37**, 351 (1986).
[12]B. H. Zimm, J. Chem. Phys. **16**, 157 (1948).
[13]A. Guinier and G. Fournet, *Small-Angle Scattering of X-Rays* (Wiley, New York, 1955).
[14]P. Debye, J. Appl. Phys. **15**, 338 (1944).
[15]O. Kratky, Kolloid Z. Z. Polym. **182**, 7 (1962).
[16]R. G. Kirste, University of Mainz, Jahresbericht des Sonderforschungsbereiches **41**, 547 (1970).
[17]G. D. Wignall, Imperial Chemical Industries Corporate Laboratory, Memorandum No. PPR GI9, 1970 (unpublished).
[18]J. Schelten, Kerntechnik **14**, 86 (1972).
[19]K. Ibel, J. Appl. Crystallogr. **9**, 196 (1976).
[20]L. E. Alexander, *X-Ray Methods in Polymer Science* (Krieger, London, 1969).
[21]*Polymer Handbook*, edited by J. Brandrup and E. H. Immergut (Wiley-Interscience, New York 1975), Chap. 4.
[22]*International Tables for X-Ray Crystallography*, edited by C. H. Macgillavry and G. D. Rieck (Kynoch, Birmingham, 1968), Chap. 3.
[23]P. J. Flory, *Principles of Polymer Chemistry* (Cornell University Press, Ithaca 1969), p. 426.
[24]P. J. Flory *Statistical Mechanics of Chain Molecules*(Wiley-Interscience, New York1968) p. 34.
[25]J. P. Cotton, B. Farnoux, G. Jannink, J. Mons, and C. Picot, C. R. Seances Acad. Sci., Ser. C **275**, 175 (1972).
[26]R. G. Kirste, W. A. Kruse, and J. Schelten, Makromol. Chem. **162**, 299 (1973).
[27]D. G. H. Ballard, G. D. Wignall, and J. Schelten, Eur. Polym. J. **9**, 965 (1973).
[28]G. D. Wignall, D. G. H. Ballard, and J. Schelten, Eur. Polym. J. **10**, 861 (1974).
[29]H. Benoit, J. P. Cotton, D. Decker, B. Farnoux, J. S. Higgins, G. Jannink, R. Ober, and C. Picot, Nature (London) **245**, 23 (1973).
[30]G. Lieser, E. W. Fischer, and K. Ibel, J. Polym. Sci., Polym. Lett. Ed. **13**, 39 (1975).
[31]R. G. Kirste, W. A. Kruse, and K. Ibel, Polymer **16**, 120 (1975).
[32]J. Schelten, D. G. H. Ballard, G. D. Wignall, G. Longman, and W. Schmatz, Polymer **27**, 751 (1976).
[33]F. S. Bates, Wignall, and W. C. Koehler, Phys. Rev. Lett. **55**, 2425 (1985).
[34]F. S. Bates, S. B. Dierker, and G. D. Wignall, Macromolecules **19**, 1938 (1986).
[35]H. Hayashi, P. J. Flory, and G. D. Wignall, Macromolecules **16**, 1328 (1983).
[36]K. P. McAlea, Macromolecules **18**, 477 (1985).
[37]J. M. O'Reilly, D. M. Teegarden, and G. D. Wignall, Macromolecules **18**, 2747 (1985).
[38]B. K. Annis, M. H. Kim, G. D. Wignall, O. Borodin, and G. D. Smith, Macromolecules **33**, 7544 (2000).
[39]D. Yoon and P. J. Flory, Macromolecules **9**, 294 (1976).
[40]J. S. Higgins and H. Benoit, *Neutron Scattering from Polymers* (Clarendon, Oxford, 1994).
[41]*Applications of Neutron Scattering to Soft Condensed Matter*, edited by B. J. Gabrys, (Gordon and Breach, New York, 2000).
[42]H. S. Ashbaugh, A. Radulescu, R. K. Prud'homme, D. Schwahn, D. Richter, and L. J. Fetters, Macromolecules **35**, 7044 (2002).
[43]D. Schwahn, D. Richter, M. Lin, and L. J. Fetters, Macromolecules **35**, 3762 (2002).
[44]E. K. Lin and A. P. Gast, Macromolecules **29**, 4432 (1996).
[45]D. Richter *et al.*, Macromolecules **30**, 1053 (1997).
[46]D. Schwahn, D. Richter, P. J. Wright, C. Symon, L. J. Fetters, and M. Lin, Macromolecules **35**, 861 (2002).
[47]H. S. Ashbaugh, L. J. Fetters, D. H. Adamson, and R. K. Prud'homme, J. Rheol. **46**, 763 (2002).
[48]H. S. Ashbaugh, X. Guo, D. Schwahn, R. K. Prud'homme, D. Richter, and L. J. Fetters, Energy Fuels **19**, 138 (2005).
[49]W. Leube, M. Monkenbush, D. Schneiders, D. Richter, D. Adamson, L. J. Fetters, P. Dounis, and R. Lovegrove, Energy Fuels **14**, 419 (2000).
[50]A. Radulescu, D. Schwahn, L. J. Fetters, and D. Richter, Appl. Phys. A: Mater. Sci. Process. **74**, S411 (2002).
[51]A. Radulescu, D. Schwahn, M. Monkenbusch, L. J. Fetters, and D. Richter, J. Polym. Sci., Part B: Polym. Phys. **42**, 3113 (2004).
[52]A. Radulescu, D. Schwahn, D. Richter, and L. J. Fetters, J. Appl. Crystallogr. **36**, 995 (2003).
[53]J. L. Fulton *et al.*, Langmuir **11**, 4241 (1995).
[54]K. P. Johnston K. L. Harrison, M. J. Clarke, S. M. Howdle, M. P. Heitz, F. V. Bright, C. Carlier, and T. W. Randolph, Science **271**, 624 (1996).
[55]J. S. Keiper, R. Simhan, J. M. DeSimone, G. D. Wignall, Y. B. Melnichenko, and H. Frielinghaus, J. Am. Chem. Soc. **124**, 1834 (2002).
[56]J. S. Keiper *et al.*, Langmuir **20**, 1065 (2004).
[57]G. J. McFann, K. P. Johnston, and S. M. Howdle, AIChE J. **40**, 543 (1994).
[58]K. A. Consani and R. D. Smith, J. Supercrit. Fluids **3**, 51 (1990).
[59]Z. T. Liu and C. Erkey, Langmuir **17**, 274 (2001).
[60]D. C. Steytler, E. Rumsey, M. Thorpe, J. Eastoe, and A. Paul, Langmuir **17**, 7948 (2001).
[61]M. J. Clarke, K. L. Harrison, K. P. Johnston, and S. M. Howdle, J. Am. Chem. Soc. **119**, 6399 (1997).
[62]S. R. da Rocha and K. P. Johnston, Langmuir **16**, 3690 (2000).
[63]S. Salaniwal, S. T. Cui, P. T. Cummings, and H. D. Cochran, Langmuir **15**, 5188 (1999).
[64]C. T. Lee, P. A. Psathas, K. J. Ziegler, K. P. Johnston, H. J. Dai, H. D. Cochran, Y. B. Melnichenko, and G. D. Wignall, J. Phys. Chem. B **104**, 11094 (2000).
[65]C. T. Lee, K. P. Johnston, H. J. Dai, H. D. Cochran, Y. B. Melnichenko, and G. D. Wignall, J. Phys. Chem. B **105**, 3540 (2001).
[66]J. Eastoe, Z. Bayazit, S. Martel, D. C. Steytler, and R. K. Heenan, Langmuir **12**, 1423 (1996).
[67]K. Nagashima, C. T. Lee, B. Xu, K. P. Johnston, J. M. DeSimone, and C. S. Johnson, J. Phys. Chem. B **107**, 1962 (2003).
[68]B. Xu, G. W. Lynn, Y. B. Melnichenko, G. D. Wignall, J. B. McClain, J. M. DeSimone and C. S. Johnson, J. Chem. Phys. **109**, 10261 (2005).

[69] S. Senapati and M. L. Berkowitz, J. Chem. Phys. **118**, 1937 (2003).
[70] J. Eastoe, A. Downer, A. Paul, D. C. Steytler, E. Rumsey, J. Penfold, and R. K. Heenan, Phys. Chem. Chem. Phys. **2**, 5235 (2000).
[71] A. Guinier, and G. Fournet, *Small-Angle Scattering of X-Rays* (Wiley, New York, 1955).
[72] J. McClain *et al.*, Science **274**, 2049 (1996).
[73] F. Triolo *et al.*, Langmuir **16**, 416 (2000).
[74] P. Wiltzius, Phys. Rev. Lett. **58**, 710 (1987).
[75] R. G. Zielinski, S. R. Kline, E. W. Kaler, and N. Rostov, Langmuir **13**, 3934 (1997).
[76] X. Dong, C. Erkey, H. J. Dai, H. C. Li, H. D. Cochran, and J. S. Lin, Ind. Eng. Chem. Res. **41**, 1038 (2002).
[77] E. Caponetti, D. Chillura Martino, M. A. Floriano, R. Triolo, and G. D. Wignall, Langmuir **11**, 2464 (1995).
[78] G. D. Wignall, J. Phys.: Condens. Matter **11**, R157 (1999).
[79] J. D. Londono *et al.*, J. Appl. Crystallogr. **30**, 690 (1997).
[80] A. I. Cooper *et al.*, Nature (London) **389**, 368 (1997).
[81] D. Hanson, Chem. Eng. News **77**, 10 (1999).
[82] P. Lindner and G. D. Wignall, MRS Bull. **24**, 34 (1999).
[83] B. Jakobs, T. Sottmann, R. Strey, J. Allgaier, L. Willner, and D. Richter, Langmuir **15**, 6707 (1999).
[84] H. Endo, J. Chem. Phys. **115**, 580 (2001).
[85] G. E. Bacon, *Neutron Diffraction* (Clarendon, Oxford, 1975) p. 561.
[86] G. Gompper and M. Schick, Phys. Rev. E **49**, 1478 (1994).
[87] N. F. Berk, Phys. Rev. A **44**, 5069 (1991).
[88] M. Teubner, Europhys. Lett. **14**, 403 (1991).
[89] P. Pieruschka and S. Marcelja, J. Phys. II **2**, 235 (1992).
[90] H. Endo, Physica B **385-386**, 682 (2006).
[91] L. W. Hrubesh, L. E. Keene, and V. R. Latorre, J. Mater. Res. **8**, 1736 (1993).
[92] J. D. F. Ramsay, Adv. Colloid Interface Sci., **76-77**, 13 (1998).
[93] W. L. Wu, W. E. Wallace, E. K. Lin, G. W. Lynn, C. J. Glinka, E. T. Ryan, and H. M. Ho, J. Appl. Phys. **87**, 1193 (2000).
[94] P. Debye, H. R. Anderson, and H. Brumberger, J. Appl. Phys. **28**, 679 (1957).
[95] R. C. Hedden, H. J. Lee, and B. J. Bauer, Langmuir **20**, 416 (2004).
[96] R. C. Hedden, H. J. Lee, C. L. Soles, and B. J. Bauer, Langmuir **20**, 6658 (2004).
[97] M. S. Silverstein, B. J. Bauer, R. C. Hedden, H. J. Lee, and B. G. Landes, Macromolecules **39**, 2998 (2006).
[98] B. D. Vogt *et al.*, Chem. Mater. **17**, 1398 (2005).
[99] M. H. Kim, C. J. Glinka, S. A Grot, and W. G. Grot, Macromolecules **39**, 4775 (2006).
[100] M. E. Kainourgiakis, T. A. Steriotis, E. S. Kikkinides, G. C. Charalambopoulou, J. D. F. Ramsay, and A. K. Stubos, Chem. Phys. **317**, 298 (2005).
[101] J. T. Wescott, Y. Qi, L. Subramanian, and T. W. Capehart, J. Chem. Phys. **124**, 134702 (2006).
[102] S. Sircar, in *Engineering Handbook*, edited by R. C. Dorf, (CRC, Boca Raton, FL, 1996).
[103] S. B. Dierker and P. Wiltzius, Phys. Rev. Lett. **66**, 1185 (1991).
[104] M. Y. Lin, S. K. Sinha, J. M. Drake, X. Wu, P. Thiyagarajan, and H. B. Stanley, Phys. Rev. Lett. **72**, 2207 (1994).
[105] B. J. Frisken, D. S. Cannels, M. Y. Lin, and S. K. Sinha, Phys. Rev. E, **51**, 5866 (1995).
[106] F. Formisano and J. Teixeira, J. Phys.: Condens. Matter, **12**, 351 (2000).
[107] G. Rother, D. Woywod, M. Schoen, and G. H. Findenegg, J. Chem. Phys. **120**, 11864 (2004).
[108] Y. B. Melnichenko, G. D. Wignall, D. R. Cole, and H. Frielinghaus, Phys. Rev. E **69**, 057102 (2004).
[109] Y. B. Melnichenko, G. D. Wignall, D. R. Cole, and H. Frielinghaus, J. Chem. Phys. **124**, 204711 (2006).
[110] W. L. Wu, Polymer **23**, 1907 (1982).
[111] G. Rother, Y. B. Melnichenko, G. D. Wignall, D. R. Cole, and H. Frielinghaus, J. Phys. Chem. (submitted).
[112] M. E. Fisher and P. G. De Gennes, C. R. Seances Acad. Sci., Ser. B **287**, 207 (1978).
[113] A. Maciolek, A. Ciach, and R. J. Evans, Chem. Phys. **108**, 9765 (1998).
[114] A. Maciolek, R. J. Evans, and N. B. Wilding, Phys. Rev. E **60**, 7105 (1999).
[115] C. M. White, Energy Fuels **19**, 659 (2005).
[116] H. W. Kroto, J. R. Heath, S. O'Brian, R. E. Curl, and R. E. Smalley, Nature (London) **318**, 162 (1985).
[117] S. Iijima, Nature (London) **354**, 56 (1991).
[118] K. A. Affholter, S. J. Henderson, G. D. Wignall, G. J. Bunick, R. E. Haufler, and R. N. Compton, J. Chem. Phys. **99**, 9224 (1993).
[119] F. Migliardo, V. Magazu, and M. Migliardo, J. Mol. Liq. **110**, 3 (2004).
[120] Y. B. Melnichenko, G. D. Wignall, R. N. Compton, and G. Bakale, J. Chem. Phys. **111**, 4724 (1999).
[121] S. Spooner, J. L. Zaretsky, and K. A. Affholter, Mater. Res. Soc. Symp. Proc. **359**, 543 (1995).
[122] M. V. Avdeev *et al.*, Langmuir **20**, 4363 (2004).
[123] L. Vaisman, G. Marom, and H. D. Wagner, Adv. Funct. Mater. **16**, 357 (2006).
[124] B. J. Bauer, E. K. Hobbie, and M. L. Becker, Macromolecules **39**, 2637 (2006).
[125] D. Schaefer, J. M. Brown, D. P. Anderson, J. Zhao, K. Chokalingam, D. Tomlin, and J. Ilavsky, J. Appl. Crystallogr. **36**, 553 (2003).
[126] D. Schaefer, J. Zhao, J. M. Brown, D. P. Anderson, and D. W. Tomlin, Chem. Phys. Lett. **375**, 369 (2003).
[127] W. Zhou, M. F. Islam, H. Wang, D. L. Ho, A. G. Yodh, K. I. Winey, and J. E. Fischer, Chem. Phys. Lett. **384**, 185 (2004).
[128] H. Wang, W. Zhou, D. L. Ho, K. I. Winey, J. E. Fischer, C. J. Glinka, and E. K. Hobbie, Nano Lett. **4**, 1789 (2004).
[129] R. Shvartzman-Cohen, Y. Levi-Kalisman, E. Nativ-Roth, and R. Yerushalmi-Rozen, Langmuir **20**, 6085 (2004).
[130] Y. Dror, W. Pyckhout-Hintzen, and Y. Cohen, Macromolecules **38**, 7828 (2005).
[131] U. Bonse and M. Hart, Appl. Phys. Lett. **7**, 238 (1965).
[132] D. Schwahn, G. Meier, and T. Springer, J. Appl. Crystallogr. **24**, 568 (1991).
[133] A. Miksovsky, H. Amenitch, H. Rauch, and E. Seidel, Phys. Status Solidi A **130**, 365 (1992).
[134] M. M. Agamalian, G. D. Wignall, and R. Triolo, J. Appl. Crystallogr. **30**, 345 (1997).
[135] M. Agamalian, D. K. Christen, A. R. Drews, C. J. Glinka, H. Matsuoka, and G. D. Wignall, J. Appl. Crystallogr. **31**, 235 (1998).
[136] J. G. Barker, C. J. Glinka, J. J. Moyer, M. H. Kim, A. R. Drew, and M. Agamalian, J. Appl. Crystallogr. **38**, 1004 (2005).
[137] J. M. Carpenter, M. Agamalian, K. C. Littrell, P. Thiyagarajan, and C. Rehm, J. Appl. Crystallogr. **36**, 763 (2003).
[138] D. W. Schaefer and M. M. Agamalian, Curr. Opin. Solid State Mater. Sci. **8**, 39 (2004).
[139] M. M. Agamalian, Notiziario Neutroni e Luce di Sinchrotrone **10**, 22 (2005).
[140] T. Kanaya, H. Takeshida, Y. Nishikoji, M. Ohkura, K. Nishida, and K. Kaji, Supramol. Sci. **5**, 215 (1998).
[141] H. Takeshita, T. Kanaya, K. Nishida, and K. Kaji, Phys. Rev. E **61**, 2125 (2000).
[142] E. H. Lehmann, P. Vontobel, and K. Kardjilov, Appl. Radiat. Isot. **61**, 503 (2004).
[143] H. Berger, Appl. Radiat. Isot. **61**, 437 (2004).
[144] W. J. Richards, M. R. Gibbons, and K. C. Shields, Appl. Radiat. Isot. **61**, 551 (2004).
[145] P. Vontobel, E. Lehmann, and W. D. Carlson, IEEE Trans. Nucl. Sci. **52**, 338 (2005).
[146] B. Schillinger *et al.*, Nucl. Instrum. Methods Phys. Res. A **542**, 142 (2005).
[147] B. Schilliger, E. Calzada, and K. Lorenz, Solid State Phenom. **112**, 61 (2006).
[148] R. Hassanein, H. O. Meyer, A. Carminati, M. Estermann, E. Lehmann, and P. Vontobel, J. Phys. D **39**, 4284 (2006).
[149] F. C. De Beer, W. J. Strydom, and E. J. Griesel, Appl. Radiat. Isot. **61**, 617 (2004).
[150] J. Rant, Z. Milic, J. Istenic, T. Knific, I. Lengar, and A. Rant, Appl. Radiat. Isot. **64**, 7 (2004).
[151] J. Rant and R. Ilic, At. Energy Rev. **15**, 327 (1977).
[152] D. A. Bostain, J. S. Brenizer, and P. M. Norris, Res. Nondestruct. Eval. **14**, 47 (2002).
[153] R. J. Bellows, M. Y. Lin, M. Arif, A. K. Thompson, and D. Jacobson, J. Electrochem. Soc. **146**, 1099 (1999).
[154] R. Satija, D. L. Jacobson, M. Arif, and S. A. Werner, J. Power Sources **129**, 238 (2004).
[155] D. Kramer, E. Lehmann, G. Frei, P. Vontobel, A. Wokman, and G. G. Scherer, Nucl. Instrum. Methods Phys. Res. A **542**, 52 (2005).
[156] N. Pekula, K. Heller, P. A. Chuang, A. Turhan, M. M. Mench, J. S. Brenizer, and K. Unlu, Nucl. Instrum. Methods Phys. Res. A **542**, 134 (2005).

[157] J. B. Zhang, D. Kramer, R. Shimoi, Y. Ona, E. Lehmann, A. Wokaun, K. Shinohara, and G. G. Scherer, Electrochim. Acta **51**, 2715 (2006).
[158] M. A. Hickner, N. P. Siegel, K. S. Chen, D. N. McBrayer, D. S. Hussey, D. L. Jacobson, and M. Arif, J. Electrochem. Soc. **153**, A902 (2006).
[159] A. Turhan, K. Heller, J. S. Brenizer, and M. M. Mench, J. Power Sources **160**, 1195 (2006).
[160] D. J. Ludlow *et al.*, J. Power Sources **162**, 271 (2006).
[161] G. D. Wignall, H. Benoît, T. Hashimoto, J. S. Higgins, S. King, T. P. Lodge, K. Mortensen, and A. J. Ryan, Macromol. Symp. **190**, 185 (2002).
[162] J. Schelten, *Scattering Techniques Applied to Supramolecular and Nonequilibrium Systems*, NATO Advanced Studies Institute, Series B: Physics, edited by S. H. Chen, B. Chu, and R. Nossal (Plenum, New York, 1981), Vol. 73, p. 75.
[163] K. Ibel, J. Appl. Crystallogr. **9**, 196 (1976).
[164] H. Maier-Leibnitz and T. Springer, Annu. Rev. Nucl. Sci. **16**, 207 (1966).
[165] D. Richter and T. Springer, A twenty years look forward at neutron scattering, ESF-OECD technical report, 1998; http//www.oecd.org/dataoecd/32/60/1904136.pdf
[166] http://www.sns. gov/
[167] http://www.isis.rl.ac.uk/targetstation2/
[168] Proceedings of the European Science Foundation Workshop, "Scientific prospects for neutron scattering with present and future sources," Autrans, France, 11–13, 1996.
[169] B. Alefeld, D. Schwahn, and T. Springer, Nucl. Instrum. Methods Phys. Res. A **274**, 210 (1989).
[170] B. Alefeld, C. Hayes, F. Mezei, D. Richter, and T. Springer, Physica B **236**, 1052 (1997).
[171] R. M. Moon, *Neutron Scattering in the Nineties* (IAEA, Vienna, 1985), Paper No. CN-46, P. 119.
[172] R. S. Stein, *Neutron Scattering in the Nineties* (IAEA, Vienna, 1985), Paper No. CN-46, P. 335.